

1  
2  
3  
4 **Use of an Imaging Spectrometer for Characterization of a Cesium Dosimeter**  
5  
6 **Calibration Facility**  
7

8  
9 Roger J. Champion, Robert M. Golduber, Kimberlee J. Kearfott\*  
10

11  
12  
13  
14 Corresponding author: Kimberlee J. Kearfott, Department of Nuclear Engineering and  
15  
16 Radiological Sciences, University of Michigan, 2355 Bonisteel Boulevard, Ann Arbor,  
17  
18 Michigan 48109-2109 USA  
19  
20

21  
22  
23  
24 e-mail: kearfott@umich.edu; Telephone: 1 (734) 763-9117; Fax: 1 (734) 763-4540  
25  
26  
27

28  
29 **Abstract**  
30

31  
32 Past investigations into the characterization of a space-constrained  $^{137}\text{Cs}$  dosimetry  
33  
34 calibration facility did not provide detailed positional measurements of gamma ray spectra.  
35  
36 In this paper, a commercially available Compton imaging system, or imaging spectrometer,  
37  
38 was used to accomplish this. This resulted in both spectral information and point of origin  
39  
40 information for the measured gamma rays. The relationship between measured spectra  
41  
42 and position was explored relative to a dosimetry phantom. The Compton equation was  
43  
44 found to accurately describe the relationship for positions associated with larger scattering  
45  
46 angles and was found to be less reliable for those associated with smaller angles.  
47  
48  
49  
50

51  
52  
53  
54 **Keywords:** phantom, virtual radionuclides, Compton scatter, Compton camera, Cadmium  
55  
56 Zinc Telluride  
57  
58  
59  
60  
61  
62  
63  
64  
65

## Introduction

The characterization of a recently commissioned space-constrained  $^{137}\text{Cs}$  dosimetry calibration facility was the subject of a prior paper (Mapes et al. 2018). That previous work was restricted to measurements of the air kerma at a set of locations in the immediate vicinity, often within 10 cm or less, of a phantom used in dosimeter calibration.

Additionally, detailed positional spectra were not reported. With such knowledge, objects could be exposed to different spectra by placing them at different locations in the room, enabling research on detector response as a function of energy. Furthermore, the work did not reveal the point of origin of photons, which could have been scattered from a variety of locations in the room. Such information would give insight into the behavior of the actual radiation field generated by the source, including both the primary photon beam and scattered photons generated through interaction of the beam with the environment. The importance of the introduction, rearrangement, or removal of objects from the room, which has a 10 m<sup>2</sup> footprint, on the radiation fields in such a small space could also be determined. The goal of this work is to provide a map of radiation spectra in the facility, accompanied by information where scattered radiation reaching those locations originated.

An imaging spectrometer, sometimes called a Compton camera, is ideal for the characterization of the spectra and understanding of the origination of scattered photons within a space such as a  $^{137}\text{Cs}$  dosimetry facility. This device utilizes the Compton scattering of gamma rays within the detector to determine their region of origin (Everett et al. 1977). One such camera utilized within this paper is the H3D H100 (H100<sup>TM</sup>, H3D Inc., Ann Arbor, MI, USA; [www.h3dgamma.com](http://www.h3dgamma.com)). This imaging spectrometer comes with software that can

1  
2  
3  
4 recognize many common gamma-emitting radionuclides based on measured photopeaks.  
5  
6 This same software facilitates the creation of “virtual radionuclides” which enable the  
7  
8 camera to recognize peaks with user defined characteristic energies. This approach was  
9  
10 first developed and demonstrated experimentally using a prototype imaging spectrometer  
11  
12 (Frank and Kearfott 2017) within a now decommissioned facility (Boria et al. 2016;  
13  
14 Studenski et al. 2007). The spectral imaging functionality was later added to the  
15  
16 commercially available software. The Compton camera experiment previously mentioned  
17  
18 was conducted to determine the effectiveness with which the camera model used could  
19  
20 measure radiation scatter off phantoms. The conclusion of the original paper was that it  
21  
22 was effective; however, the camera was considered a prototype and had a misaligned photo  
23  
24 camera relative to the Compton camera. This consistently led to gamma rays being  
25  
26 indicated as coming from positions lower and further to the viewer's left than where they  
27  
28 actually were known to originate. Additionally, there were inconsistencies between the  
29  
30 angles associated with the peaks. This paper seeks to either correct or explain the  
31  
32 previously observed departure from expected values and to provide images of the  
33  
34 scattered photons that are aligned with the photo camera in a facility which was previously  
35  
36 not characterized in this fashion.  
37  
38  
39  
40  
41  
42  
43  
44  
45

## 46 **Background**

47  
48 The energy spectra of scattered photons are spatially dependent because the energy  
49  
50 of a scattered photon is dependent on the angle at which it scattered off a given target.  
51  
52

53 Mathematically the scattered photon energy,  $E_2$ , is given by:  
54  
55

$$56 E_2 = \frac{E_1}{1 + \left(\frac{E_1}{m_e c^2}\right)(1 - \cos \theta)} \quad (1)$$

57  
58  
59  
60  
61  
62  
63  
64  
65

1  
2  
3  
4 where  $E_1$  is the incident energy, and  $\theta$  is the half angle of the cone formed (Everett et al.  
5  
6  
7 1977). The relationship between  $E_2$  and  $\theta$  is illustrated by the curve in Fig. 1. Compton  
8  
9 imaging is achieved through the measurement of a single gamma ray that scattered once  
10  
11 within a single crystal or crystal array before being absorbed within the material. A cone of  
12  
13 likely directions of origin can be back-projected using the energy upon scatter, energy upon  
14  
15 absorption, location of scatter, location of absorption and Equation 1. As more particles are  
16  
17 measured, a region of crossover of the cones can be determined, and this is considered the  
18  
19 most likely position of the source. Because it has a large band gap which allows it to remain  
20  
21 sensitive to radiation at room temperature (Knoll 2010), cadmium zinc telluride (CZT) is  
22  
23 the crystal or detector of choice for most imaging spectrometers. CZT also has a high  
24  
25 effective cross section for photoelectric absorption which can greatly increase its efficiency  
26  
27 as this reaction type must occur for any directional information to be determined.  
28  
29  
30  
31  
32

## 33 **Materials and Methods**

### 34 ***Imaging Spectrometer***

35  
36  
37  
38  
39 NaI(Tl) and HPGe detectors were tested as options for accurately characterizing the  
40  
41 energy spectrum at different positions in facility. Unfortunately, the systems chosen had  
42  
43 dead times exceeding 99%, rendering them unmanageable for this purpose, and they were  
44  
45 not capable of producing photographic images. All measurements conducted for this  
46  
47 investigation were performed using the H3D H100 Compton imaging spectrometer  
48  
49 (H100™, H3D Inc., Ann Arbor, MI, USA; [www.h3dgamma.com](http://www.h3dgamma.com)) shown in Fig. 2. This device  
50  
51 produces both an energy spectrum for incident photons and a visible light photograph of  
52  
53 the region in front of the camera with a heat map representing the origin of monoenergetic  
54  
55 photon radiation superimposed upon the photograph. The visible light photograph  
56  
57  
58  
59  
60  
61  
62  
63  
64  
65

1  
2  
3  
4 provided is a regular photograph replicating the spectrum of light visible to humans. A heat  
5  
6 map of the gamma rays originating outside the field of view of the visible light photograph  
7  
8 is also available however it was not used in this project. The heat maps represent regions of  
9  
10 more likely origin with warmer colors. The imager has 250 keV to 3 MeV imaging and 50  
11  
12 keV to 3 MeV spectroscopy ranges. The imaging spectrometer becomes count rate-limited  
13  
14 at 5 mSv h<sup>-1</sup> for <sup>137</sup>Cs (Wahl et al. 2015). The actual medium in which the gamma ray  
15  
16 interaction occurs is a single 6 cm<sup>3</sup> crystal of CZT. The imaging spectrometer was operated  
17  
18 remotely using a tablet computer that communicated with the imaging spectrometer using  
19  
20 wireless internet.  
21  
22  
23  
24  
25

### 26 ***Measurement Environment***

27  
28  
29 As shown in Fig. 3, the dosimetry facility is a 3.8 m x 3.6 m room with a 3.4 m high  
30  
31 ceiling. The walls, floor, and ceiling consist of solid concrete. The center of the room  
32  
33 contains the table on which the phantom rests. This table is centered on and secured to a  
34  
35 raised, metallic, cylindrical plate covering a cylindrical pit previously used to house a  
36  
37 source. The plate rises ~12 cm above the floor which is not entirely level. A stack of  
38  
39 phantom material and a large wooden box containing phantom material are stored along  
40  
41 the wall directly opposite the entrance to the room from the maze. The geometry of the  
42  
43 room and the objects within the room all affect the radiation field produced when the beam  
44  
45 is generated and are potential causes of departures from expected values.  
46  
47  
48  
49  
50

### 51 ***Radioactive Source***

52  
53  
54 A 260.5 GBq <sup>137</sup>Cs dosimetry calibration source (Model 28-8A, JL Shepherd and  
55  
56 Associates, San Fernando, CA, USA, www.jlshepherd.com) was used. The 662 keV photons  
57  
58 produced by the <sup>137</sup>Cs are within the energy range in which the Compton effect is the  
59  
60  
61  
62  
63  
64  
65

1  
2  
3  
4 dominant means of interacting with elements with a Z number of about 80 or below. The  
5  
6 effective Z of CZT is approximately 43.3, which makes H3D H100 optimal for imaging the  
7  
8 primary **photon** beam from the  $^{137}\text{Cs}$  source. Beam scatter at  $\sim 110$  degrees or less may  
9  
10 also be imaged by the spectrometer. The apparatus houses a cylindrical source that is  
11  
12 stored within a shielded chamber. The source, approximately 11 cm from the edge of the  
13  
14 shielding, can be lifted by a lever to a position in front of a small rectangular window. The  
15  
16 beam then emerges from the window collimated into an approximately rectangular shape  
17  
18 with 30 degrees full angle divergence.  
19  
20  
21  
22

### 23 ***Dosimetry Phantom***

24  
25  
26 The polymethyl methacrylate (PMMA) phantom used for this experiment was a 40  
27  
28 cm x 40 cm x 15 cm rectangular prism, which was specially designed to facilitate dosimeter  
29  
30 calibration (Parker et al. 2011). Its composition is made to mimic human tissue in terms of  
31  
32 density and roughly in terms of atomic composition. Many dosimeter irradiation  
33  
34 experiments are performed with the dosimeters positioned directly in front of the phantom  
35  
36 to better simulate the environment that they will be used in, such as attached to human  
37  
38 bodies for personnel dosimetry. The phantom was positioned as shown in Fig. 3.  
39  
40  
41  
42  
43

### 44 ***General Setup***

45  
46 The imaging spectrometer was placed at 91 cm above the ground of the facility on a  
47  
48 small wheeled table. The center of the imaging spectrometer was positioned 100 cm from  
49  
50 the center of the phantom. The phantom was placed on a 60.1 cm x 60.1 cm aluminum table  
51  
52 at a height of 90 cm. One of the 40 cm x 40 cm faces of the phantom was positioned such  
53  
54 that it was facing the window of the collimator and such that the central axis of the beam  
55  
56 produced in the collimator is perpendicular to this face and passes through its center. The  
57  
58  
59  
60  
61  
62  
63  
64  
65

1  
2  
3  
4 center of this face was set at 100.4 cm from the window, a common distance for dosimetry  
5  
6 experiments. The visible light photography camera on the H3D H100 was positioned such  
7  
8 that its line of sight was toward the center of the phantom. Measurements were taken both  
9  
10 with the phantom present and absent.  
11  
12

### 13 14 ***Measurement Procedure***

15  
16 A total of three measurements were taken at each of six positions. The first  
17  
18 measurement was a 420 s background with the phantom absent. With the source raised, a  
19  
20 1,200 s measurement was then taken with the phantom present. This measurement was  
21  
22 then repeated with the phantom absent. As shown in Fig. 4, the imaging spectrometer's  
23  
24 positions were at 0, 30, 150, 180, 210, and 330 degrees on a 100 cm radius circle centered  
25  
26 on the phantom, with 270 degrees being the position of the irradiator. As Fig. 4 shows,  
27  
28 these positions are identified by an arbitrary numbering system corresponding to different  
29  
30 expected scattering angles at the center of the phantom. Based on Equation 1 and the  
31  
32 assumption that the majority of photon scattering events occurred near the center of the  
33  
34 phantom and were recorded near the center of the detector, the expected energy for the 60,  
35  
36 90, and 120 degree scattered photons would be 402 keV, 288 keV, and 225 keV  
37  
38 respectively.  
39  
40  
41  
42  
43  
44  
45

### 46 47 ***Imaging and Postprocessing***

48  
49 After the measurements were performed it was necessary to post-process the  
50  
51 spectral data using the provided software (Visualizer Ver. 2.5.10-0-g34be386; H3D Inc., Ann  
52  
53 Arbor, MI, USA; [www.h3dgamma.com](http://www.h3dgamma.com)). The software uses a library of radionuclides to  
54  
55 determine which are contributing to the spectrum, highlights and labels their peaks within  
56  
57 the spectrum, and represents their regions of origin on the image taken by the visible light  
58  
59  
60  
61  
62  
63  
64  
65

1  
2  
3  
4 camera by superimposing a heatmap. Several “virtual radionuclides” were defined, each  
5  
6 representing a different Compton scatter angle. These were used to determine the relative  
7  
8 places of origin of different single scatter events and to identify the dominant angle of scatter  
9  
10 for each given measurement position. The energy spectra were further used to identify  
11  
12 scattering angles by subtracting the count rate without the phantom from the count rate with  
13  
14 the phantom. This was meant to make the difference in the radiation field due to the addition  
15  
16 of the phantom more apparent. Peak energies associated with once scattered photons were  
17  
18 used along with an estimated FWHM to calculate the standard deviation and resolution of  
19  
20 the peaks.  
21  
22  
23  
24  
25

### 26 ***Simulation***

27  
28  
29 A simple simulation of the experiment was made using a standard Monte Carlo  
30  
31 radiation transport code, MCNP (MCNP 6.2, Los Alamos National Laboratory, Los Alamos,  
32  
33 NM, USA, [www.lanl.gov](http://www.lanl.gov)). A cone beam incident on a PMMA phantom surrounded by six 4  
34  
35 cm diameter spheres, which represent the six positions of the detector, was simulated. The  
36  
37 cone beam spread is based on the measured spread of the actual  $^{137}\text{Cs}$  beam, 30-degree full  
38  
39 angle divergence and consists solely of evenly radially distributed 662 keV gamma rays.  
40  
41 The phantom dimensions, the distance between the phantom face and beam origin point,  
42  
43 and the relative positions of all the centers of the “detectors” and the center of the phantom  
44  
45 are identical to their intended real-world positions. The six “detectors” simply record the  
46  
47 flux incident on their surfaces using the F1 tally and do not actually interact with the  
48  
49 photons as this could affect the measurements of other “detectors.” Note that the  
50  
51 simulation has all six positions measured at once whereas the real experiment involves the  
52  
53 detector being moved from position to position. The simulation does not account for any  
54  
55  
56  
57  
58  
59  
60  
61  
62  
63  
64  
65

1  
2  
3  
4 scatter within the environment other than off the PMMA phantom since this is the primary  
5  
6 object of interest. This simulation is meant to help develop a sense of how the gamma rays  
7  
8 will be affected by the phantom beyond the basic assumption that the measured peaks will  
9  
10 be associated with the angle measured between the center of the phantom and the center  
11  
12 of the detector. The general shape of the spectra and positions of the peaks are the focus of  
13  
14 this simulation. Because the actual count values do not factor into learning about these  
15  
16 qualitative characteristics of the spectra, all spectra will be normalized by dividing the  
17  
18 counts in each bin by the highest count of any bin in order to make the graphs simpler to  
19  
20 read.  
21  
22  
23  
24  
25

## 26 **Results and Discussion**

### 27 ***Measured Energy Spectra as a Function of Position with Phantom Present***

28  
29 As shown in Figs. 5 and Table 1, the energy spectra obtained from the six positions  
30  
31 show scatter peaks decreasing in energy with increasing scatter angle. At 120 degrees, the  
32  
33 energy of the peak in the measured spectra agreed well with what is expected for  
34  
35 scattering of a 662 keV pencil beam with a point scattering target, namely 225 keV. The  
36  
37 visualization software was able to recognize the user defined virtual radionuclide  
38  
39 representing the 120 degree scatter peak but could not produce a heat map because of the  
40  
41 lower energy gamma rays involved. The spectra collected at 90 degrees had the scatter  
42  
43 peaks centered around  $302 \pm 12$  keV, compared with a predicted energy of 288 keV based  
44  
45 upon a pencil beam scattering on a point medium. While only a small difference compared  
46  
47 with experimental uncertainty, this would correspond to an effective scattering angle  
48  
49 closer to about 85 degrees. Variations are expected because neither a point scattering  
50  
51 media nor a pencil beam are involved. Finally, the 60 degree scatter measurements showed  
52  
53  
54  
55  
56  
57  
58  
59  
60  
61  
62  
63  
64  
65

1  
2  
3  
4 the least agreement with the expected results with the peaks shifting toward 55 degree  
5  
6 scatter energy.  
7

### 8 9 ***Origin of Scatter Within the Phantom***

10  
11 Some evidence of the effects of attenuation can be seen in Fig. 6b and Fig 6c. In Fig. 6b,  
12  
13 observe the heat map for the scatter particles at position 2; the left edge is shifted toward  
14  
15 the half of the phantom nearer to the imaging spectrometer which would be the region  
16  
17 with the lower attenuation due to a shorter average path through the phantom. This is also  
18  
19 the energy that has the higher peak. The 60 degree scatter photons in Fig. 6c shows no such  
20  
21 spatial shift. This indicates that its representative path originates more toward the center  
22  
23 of the phantom which corresponds to a longer path through the phantom for the scattered  
24  
25 photons. Therefore more 60 degree scattered photons may have interacted again on their  
26  
27 way to the detector lowering the count rate.  
28  
29  
30  
31  
32

### 33 34 ***Scattered Energy Spectra due to Phantom Presence***

35  
36 Fig. 7 shows the difference in the count rates as a function of energy for the different  
37  
38 measured positions with and without the phantom present. These represent the scattered  
39  
40 spectra due to the phantom itself. While small negative values may arise simply because of  
41  
42 measurement uncertainty and counting statistics, larger negative values are representative  
43  
44 of a range of energies that has been reduced in energy to produce the peak seen. Though  
45  
46 this gives a good sense of how the phantom effects the environment directly it is harder to  
47  
48 determine its exact effect on backscatter. Removing the phantom, allows more primary  
49  
50 photons to hit the rest of the environment, so the room return is greater without the  
51  
52 phantom. This is likely to influence the results that would not be present if the  
53  
54 environment was not space constrained. The differences also make it clear that the count  
55  
56  
57  
58  
59  
60  
61  
62  
63  
64  
65

1  
2  
3  
4 rate for a range of energies associated with single scattered photons had increased. For  
5  
6 example, in Fig. 7c and 7d at the 90 degree positions, P3 and P4, an increase in count rate  
7  
8 for energies associated with scattered photons associated with angles from ~100 to ~120  
9  
10 can be clearly identified. Additionally, for Fig. 7e and 7f at the 60 degree positions, P1 and  
11  
12 P2, count rates for energies associated with scatter angles from ~60 to ~125 increased  
13  
14 comparably to the 55 degree energy increase with the ~105 count rates nearly surpassing  
15  
16 or surpassing the 55 degree count rate.  
17  
18  
19  
20

### 21 ***Potential Causes for Departure from Expectation***

22  
23  
24 The expectation for all positions was that a scatter peak would be observed for the  
25  
26 energy associated with the angle between the center of the phantom and the detector and  
27  
28 that the increase in scatter rate would be a high resolution highest around this energy. This  
29  
30 expectation ignores some important factors such as the beam spreading over the entirety  
31  
32 of the phantom, the rate of once scattered photons decreasing as the beam is attenuated  
33  
34 within the phantom, the size of the detector, and the different path lengths required to exit  
35  
36 the phantom and reach the detector for different angles of scatter. The fact that the peak of  
37  
38 the 90 degree scatter measurement is shifted 5 degrees down could be due to the rate of  
39  
40 single scatter being higher in the portion of the phantom closer to the source. Additionally,  
41  
42 it makes sense that of these scattered photons, those occurring in regions with shorter  
43  
44 paths through the phantom to the detector would be overrepresented as they have less of a  
45  
46 chance of being attenuated. This, in general, means scattered photons closer to the detector  
47  
48 would be overrepresented. Primary gamma rays passing through this region would have  
49  
50 departed from the central axis of the beam and would be traveling in a trajectory that has  
51  
52  
53  
54  
55  
56  
57  
58  
59  
60  
61  
62  
63  
64  
65

1  
2  
3  
4 already placed them nearer to the detector which means that the scatter that would direct  
5  
6 them into the detector would be less than 90.  
7  
8

9 All these factors help to explain the departure from initial expectations. The  
10 extreme departure from 60 degree scatter measurements could be due to factors  
11 mentioned above. The increase in energies associated with ~65 to 125 degree scattered  
12 photons could be due to multiple scatters occurring with the same photon as the position  
13 are the most forward oriented and photons that have scattered multiple times are most  
14 likely to occur as the combination of two small departures from the original trajectory. This  
15 would make sense considering angles of over 90 degrees that scattered once within the  
16 phantom would be moving away from the detector.  
17  
18  
19  
20  
21  
22  
23  
24  
25  
26  
27  
28

### 29 ***Monte Carlo Radiation Transport Simulation Results***

30  
31 The simulation also gives some insight into what should be theoretically expected.  
32 The peak for 60, 90, and 120 degrees was shifted to roughly the 45, 80, and 115 degree  
33 regions, respectively as shown in Fig. 8. This shows a consistent drop as the average path  
34 length to the detector increases, consistent with the experiment. The magnitude of the drop  
35 is higher, implying a greater overrepresentation of lower angle scattered photons. This  
36 could be due to the distribution of gamma rays in the simulation being perfectly isotropic  
37 whereas the actual beam has been shown to have a pronounced difference in the air kerma  
38 rates measured at the edges and the center of the phantom. The edges have been  
39 demonstrated to receive 10% to 50% less air kerma relative to the central position (Mapes  
40 et al. 2018). This could counter the effect of shorter beam path and lower angle of scatter  
41 preference since the portion of trajectories with these characteristics is smaller for the  
42 actual measurements.  
43  
44  
45  
46  
47  
48  
49  
50  
51  
52  
53  
54  
55  
56  
57  
58  
59  
60  
61  
62  
63  
64  
65

1  
2  
3  
4 **Conclusions**  
5

6  
7 The Compton imaging spectrometer is a useful tool for understanding the behavior  
8  
9 of the radiation field within a facility, as specifically illustrated for the space-controlled  
10  
11  $^{137}\text{Cs}$  dosimeter calibration facility characterized in this paper. Due to its unique ability to  
12  
13 provide both detailed spectra and a representation of the region of origin for photons of a  
14  
15 given energy, it is appropriate for the mapping of positionally dependent radiation field of  
16  
17 the facility. The positional energy spectral information provided by the imaging  
18  
19 spectrometer for this work may ultimately be exploited to perform instrument and  
20  
21 dosimeter calibrations at energies other than the primary beam energy of 662 keV. Because  
22  
23 of the precise visible camera alignment with the photon images, the device provides useful  
24  
25 qualitative information to understand spectral changes.  
26  
27  
28  
29  
30

31 **Acknowledgements**  
32

33  
34 This work was funded in-part by the Consortium for Verification Technology under the  
35  
36 Department of Energy National Nuclear Security Administration, award number  
37  
38 DE-NA0002534. Special thanks are extended to Daniel Shy for assistance with learning to use  
39  
40 the imaging spectrometer. The facility floorplan was modified from a diagram originally  
41  
42 provided by Long Kiu (Edgar) Chung.  
43  
44  
45

46 **References**  
47

48 Boria AJ, Rucinski BD, Abraham SA, Dawson AS, Jawad AH, Miklos JA, Kearfott KJ. Cs-137  
49  
50 dosimeter irradiation facilities: Calibration frequency, precision, and accuracy. Health Phys  
51  
52 112(4):357-363; 2017. DOI:10.1097/HP.0000000000000641.  
53  
54  
55  
56  
57  
58  
59  
60  
61  
62  
63  
64  
65

1  
2  
3  
4 Everett DB, Fleming JS, Todd RW, Nightingale JM. Gamma-radiation imaging system based  
5  
6 on the Compton effect. Proc IEE 142:995-1000; 1977. DOI:10.1049/piee.1977.0203.  
7  
8

9  
10  
11 Frank SJ, Kearfott KJ. Imaging of gamma-ray scatter from a polymethyl-methacrylate  
12  
13 phantom using a Compton imaging spectrometer. Health Phys 113(2):135-142; 2017.  
14  
15 DOI:10.1097/HP.0000000000000681.  
16  
17  
18

19  
20  
21 Knoll GF. Radiation detection and measurement. 4<sup>th</sup> ed. New Jersey: John Wiley and Sons;  
22  
23 2010.  
24  
25  
26

27  
28  
29 Mapes JL, Liu K, Abraham S A, Wilhelm AS, Latosz LV, Kearfott KJ. Setup and  
30  
31 characterization of a cesium-137 dosimetry calibration source in a space-constrained  
32  
33 environment. Health Phys 115(5):569-580; 2018. DOI:10.1097/HP.0000000000000941.  
34  
35  
36

37  
38  
39 Parker LW, Harvey JA, Kearfott KJ. An integrated system for the beta, gamma and neutron  
40  
41 calibration and storage of thermoluminescent dosimeters for a research laboratory. Health  
42  
43 Phys 100(S1):S43-S49; 2011. DOI:10.1097/HP.0b013e3181e47b11.  
44  
45  
46

47  
48  
49 Studenski MT, Haverland NP, Kearfott KJ. Simulation, design, and construction of a <sup>137</sup>Cs  
50  
51 irradiation facility Health Phys 92(5):S78-S86; 2007.  
52  
53 DOI:10.1097/01.HP.0000253943.69777.a9.  
54  
55  
56

1  
2  
3  
4  
5  
6  
7  
8  
9  
10  
11  
12  
13  
14  
15  
16  
17  
18  
19  
20  
21  
22  
23  
24  
25  
26  
27  
28  
29  
30  
31  
32  
33  
34  
35  
36  
37  
38  
39  
40  
41  
42  
43  
44  
45  
46  
47  
48  
49  
50  
51  
52  
53  
54  
55  
56  
57  
58  
59  
60  
61  
62  
63  
64  
65

Wahl CG, Kaye WR, Wang W, Zhang F, Jaworski J M, King A, Boucher YA, He Z. The Polaris-H  
imaging spectrometer. Nuclear Inst and Methods in Phys Research A 784:377–81; 2015.  
DOI:10.1016/j.nima.2014.12.110.

## LIST OF FIGURES

Figure 1: The relationship between the energy of primary scatter gammas and the angle of scatter for 662 keV gammas.

Figure 2: The H3D H100™ camera.

Figure 3: The  $^{137}\text{Cs}$  dosimetry facility, shown in a) floorplan, b) photographic view looking towards the room entrance showing phantom, source, and imaging spectrometer.

Figure 4: Representation of the experimental setup representing the relative positions of the phantom and detectors.

Figure 5: Gamma ray energy spectra, expressed as count rate, at positions (a) 60 degrees on left (P1), (b) 60 degrees on right (P2), (c) 90 degrees on left (P3), (d) 90 degrees on right (P4), (e) 120 degrees on left (P5), and (f) 120 degrees on right (P6). Peaks were expected to be 402 keV, 288 keV, and 225 keV for the 60, 90, and 120 degree positions, respectively however the observed peaks differed significantly for some positions as is illustrated by Table 1.

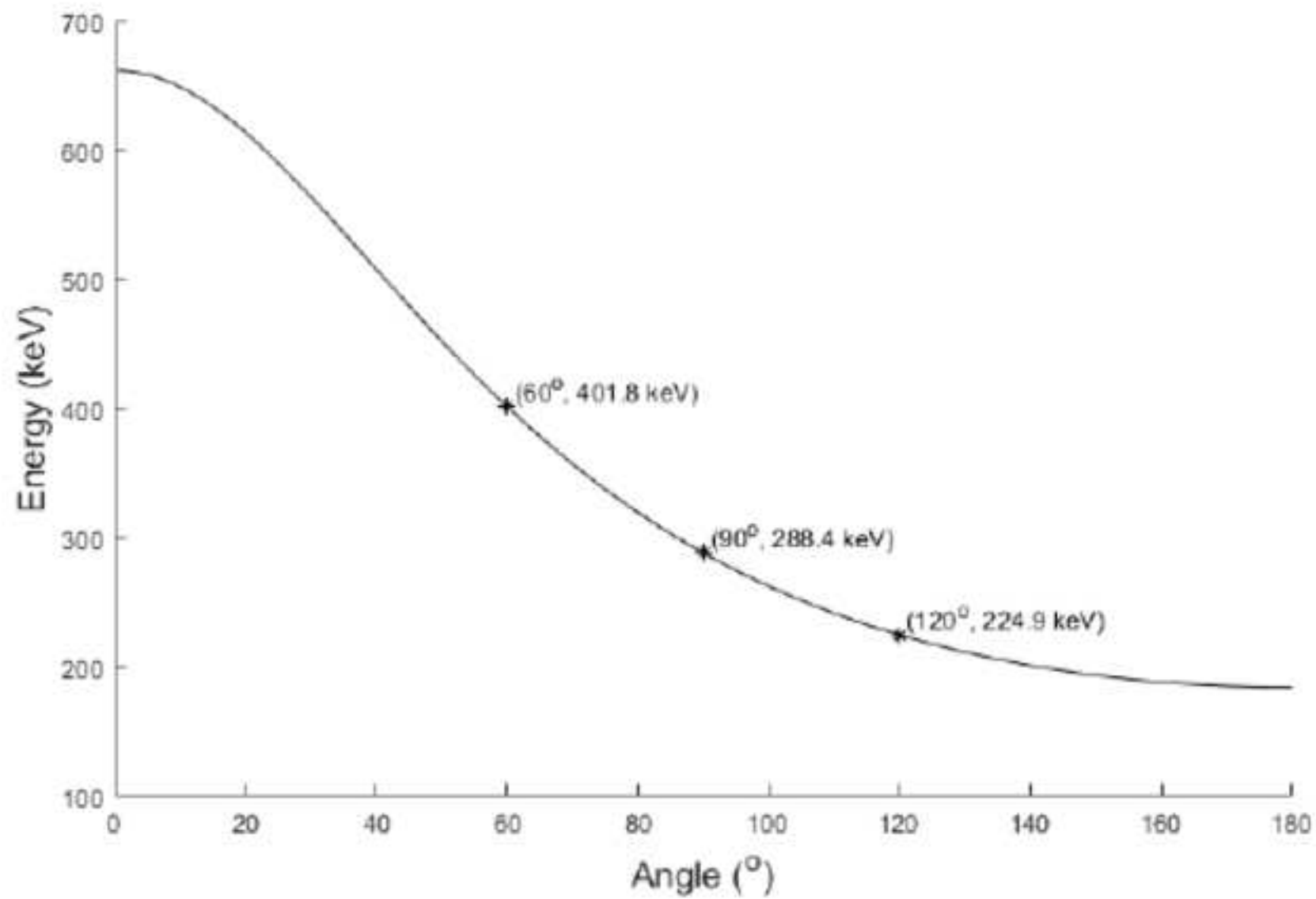
Figure 6: Heat map for gamma energy associated with (a) 45 degree, (b) 50 degree, and (c) 60 degree scattered primary photons with detector positioned at 60 degrees on left (P1). The disparity between the angle of scatter associated with the photon based on its energy and the position of the detector is due to the non-finite nature of the detector, the gamma beam, and the phantom which allows for single scattered photons of a greater range of scatter angles to reach the detector. Note the shift toward the center of the phantom from 50 degree to 60 degree.

1  
2  
3  
4 Figure 7: Difference in gamma count rate between the measurement with and the  
5  
6 measurement without phantom present, as a function of angle in degrees calculated using  
7  
8 the Compton scatter formula, at positions a) 60 degrees on left (P1), (b) 60 degrees on right  
9  
10 (P2), (c) 90 degrees on left (P3), (d) 90 degrees on right (P4), (e) 120 degrees on left (P5),  
11  
12 and (f) 120 degrees on right (P6). Peaks were expected to be around 60, 90, and 120  
13  
14 degree positions, respectively.  
15  
16  
17  
18  
19

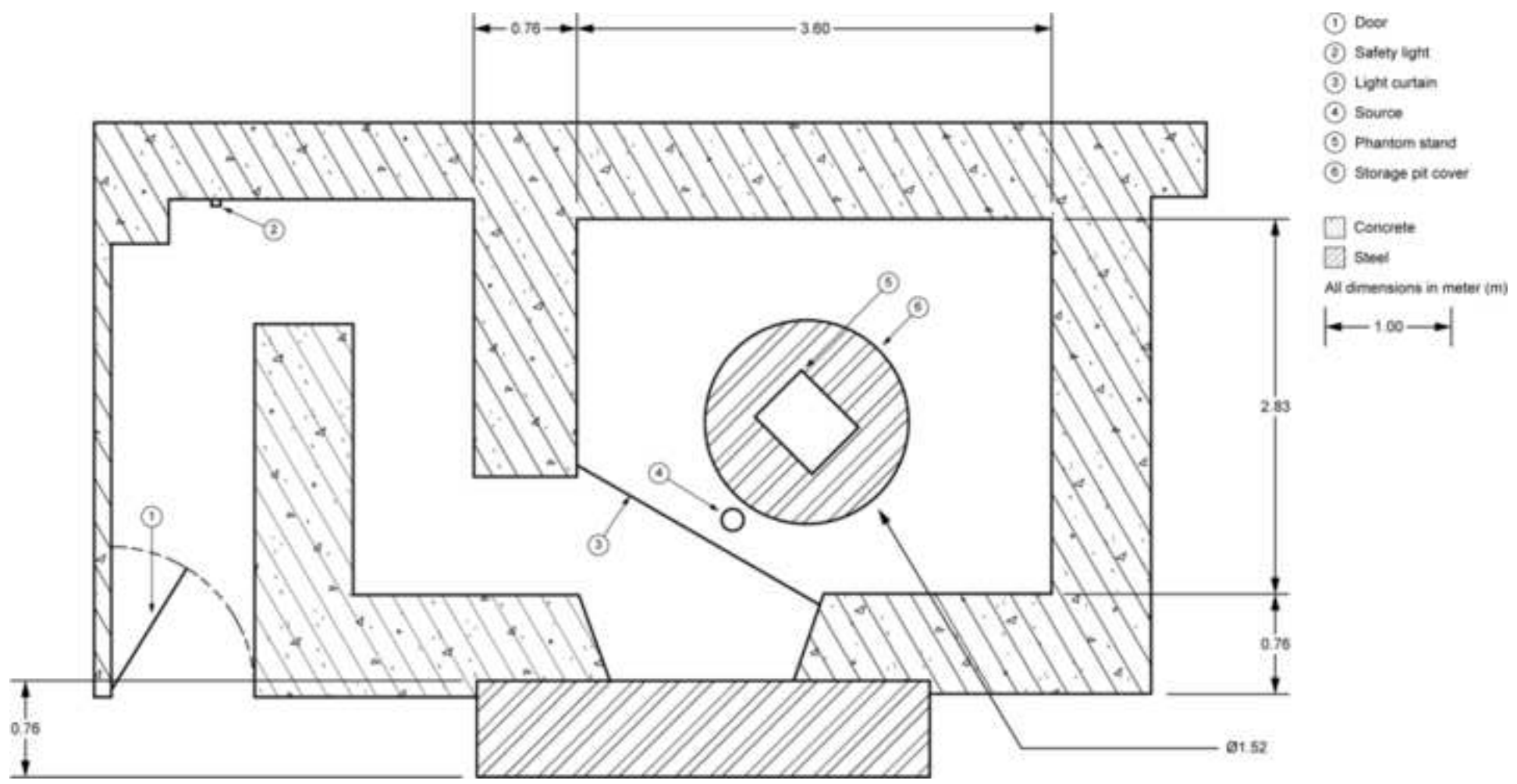
20 Figure 8: MCNP simulation energy spectra results of normalized counts with energy  
21  
22 converted into angle via the Compton scatter formula associated with positions (a) 60  
23  
24 degrees on left (P1), (b) 60 degrees on right (P2), (c) 90 degree on left (P3), (d) 90 degree  
25  
26 on right (P4), (e) 120 degree on left (P5), and (f) 120 degree on right (P6). The actual  
27  
28 counts of the energy bins were arbitrary as they were dependent on the number of  
29  
30 particles simulated, so the counts were normalized by dividing every bin's count by the  
31  
32 highest count recorded for any bin in the "detector."  
33  
34  
35  
36  
37  
38  
39  
40  
41  
42  
43  
44  
45  
46  
47  
48  
49  
50  
51  
52  
53  
54  
55  
56  
57  
58  
59  
60  
61  
62  
63  
64  
65

Table 1: A comparison of expected values with actual results for the dominant scatter peaks observed with the imaging spectrometer. The coordinate system for the spectrometer position consists of the center of the beam intersecting the center of the phantom with the spectrometer located on a circle at a 100 cm distance from the phantom center (as shown in Fig. 4). The expected scatter energy is the energy predicted using the Compton scattering equation for a point scattering volume in the center of the phantom. Scattered energies correspond to the centroids of the scattering peaks in the measured spectra, with error bars based upon the full width at half maximum for the peaks. The effective scatter angle is the angle at which 662 keV photons must have scattered in order to produce the measured scattered energy. This differs from the expected scattered energy because the phantom is an object of significant dimensions interacting with a broad beam.

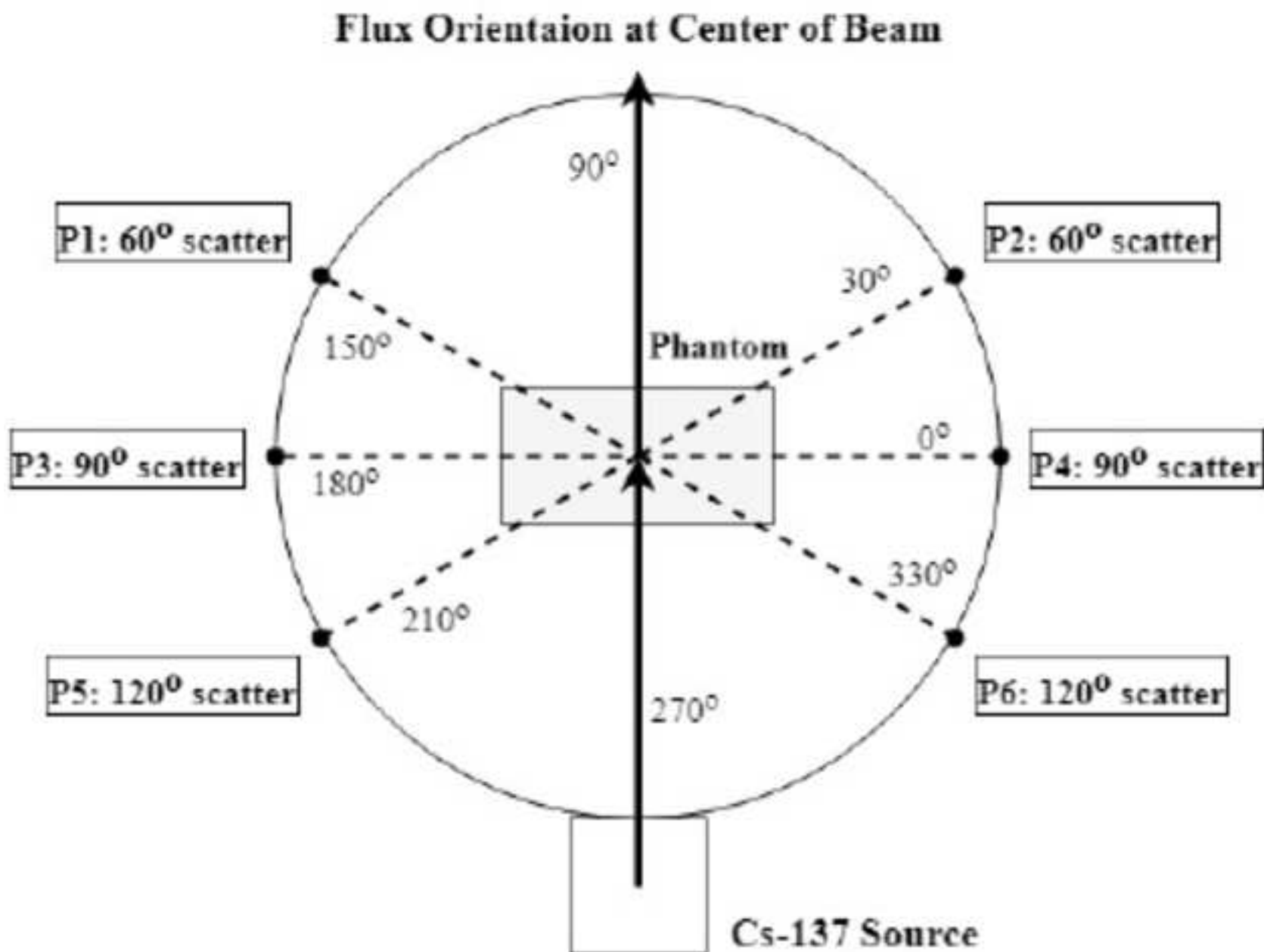
<i>Spectrometer Position</i>	<i>Spectrometer Position Angle (degrees)</i>	<i>Expected Scattered Energy (keV)</i>	<i>Measured Scattered Energy (keV)</i>	<i>% Difference in Energies</i>	<i>Resolution (%)</i>	<i>Effective Scatter Angle (degrees)</i>
P1	60	402	446 ± 20	11.3	10.3 ± 4.4	56.7
P2	60	402	462 ± 18	14.8	9.3 ± 4.0	54.9
P3	90	288	298 ± 12	4.6	9.7 ± 4.1	85.4
P4	90	288	306 ± 13	7.2	9.8 ± 4.2	84.2
P6	120	225	225 ± 6	1.8	6.2 ± 2.7	119.3
P5	120	225	229 ± 7	3.5	7.0 ± 3.0	116.7

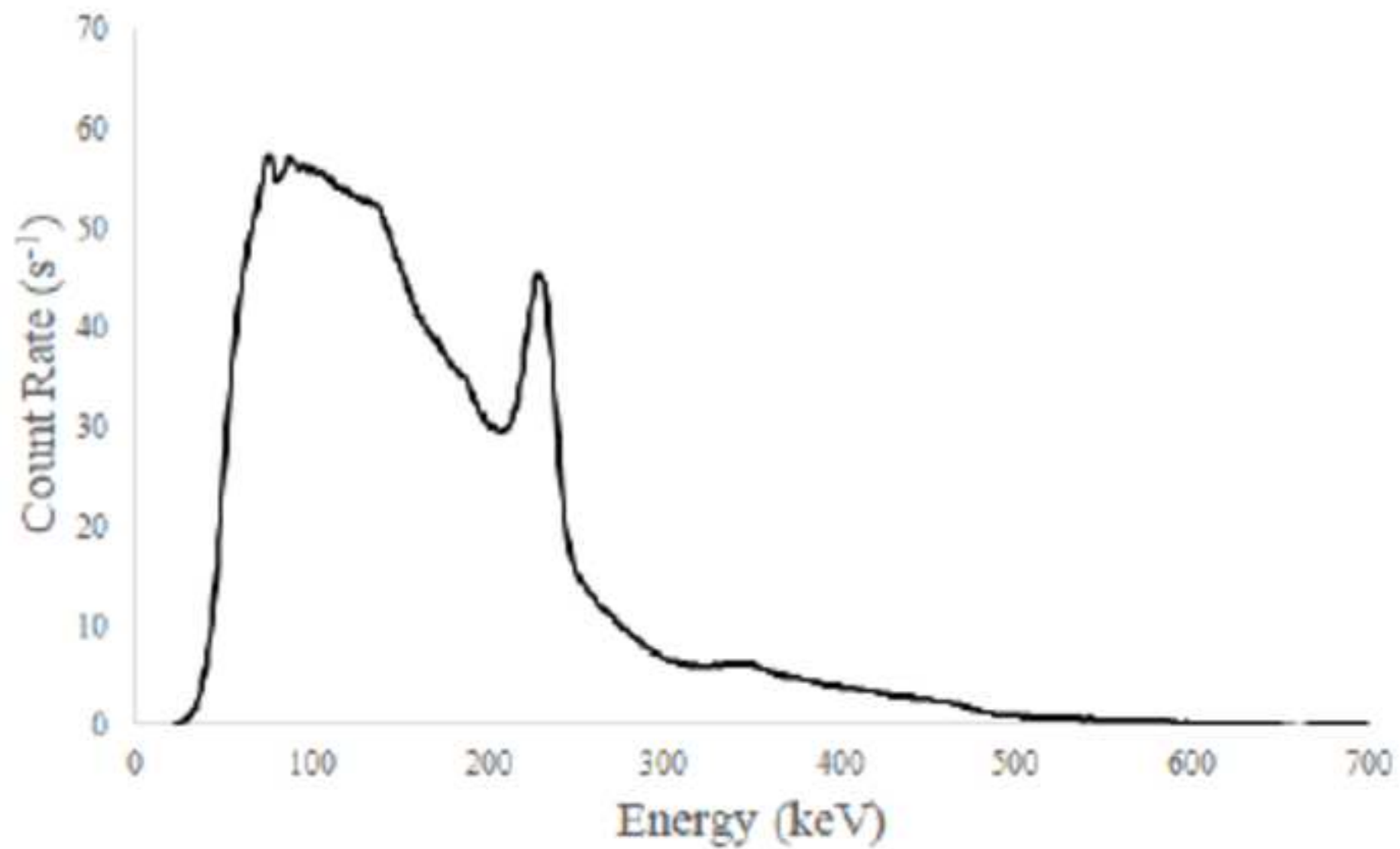


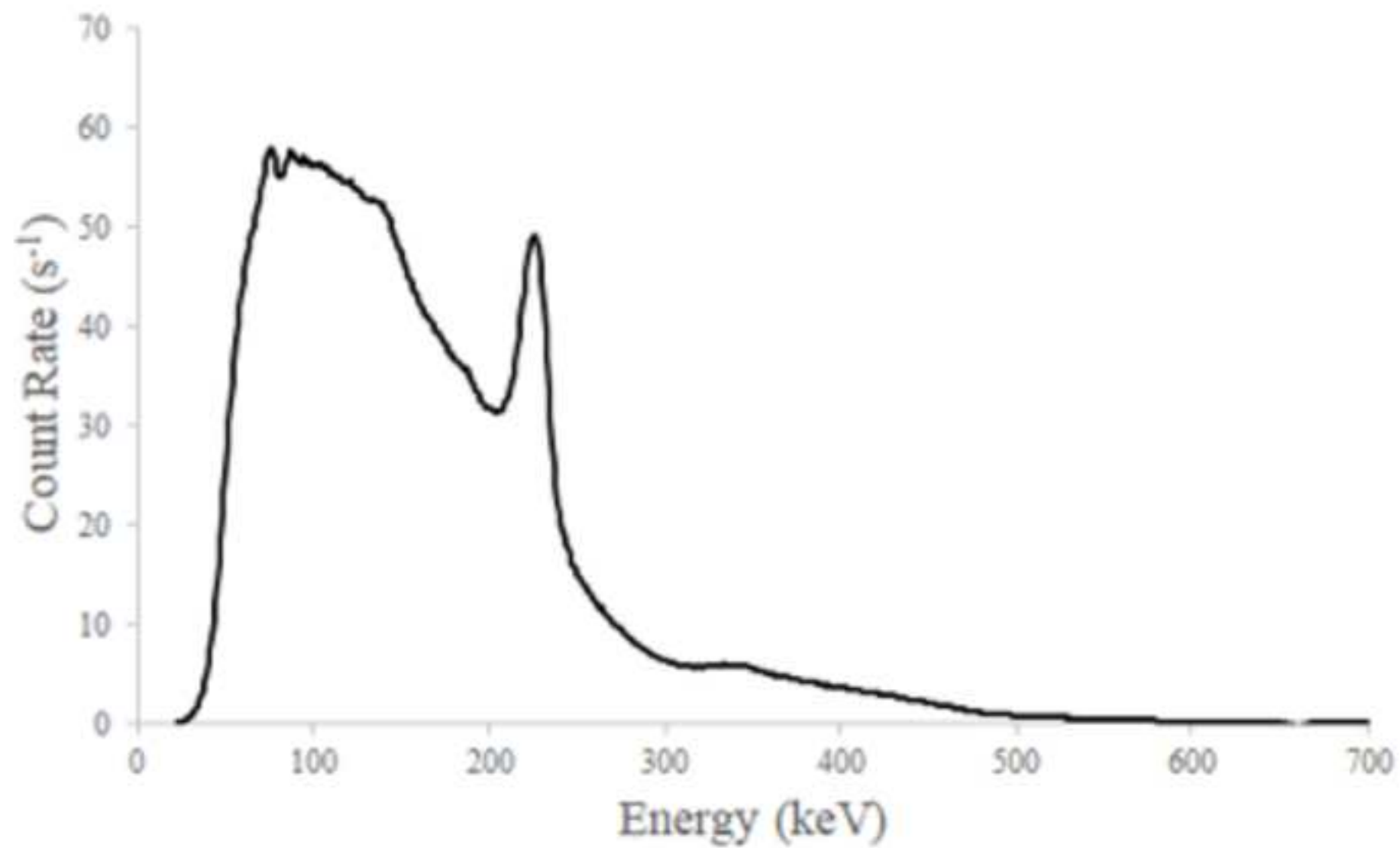


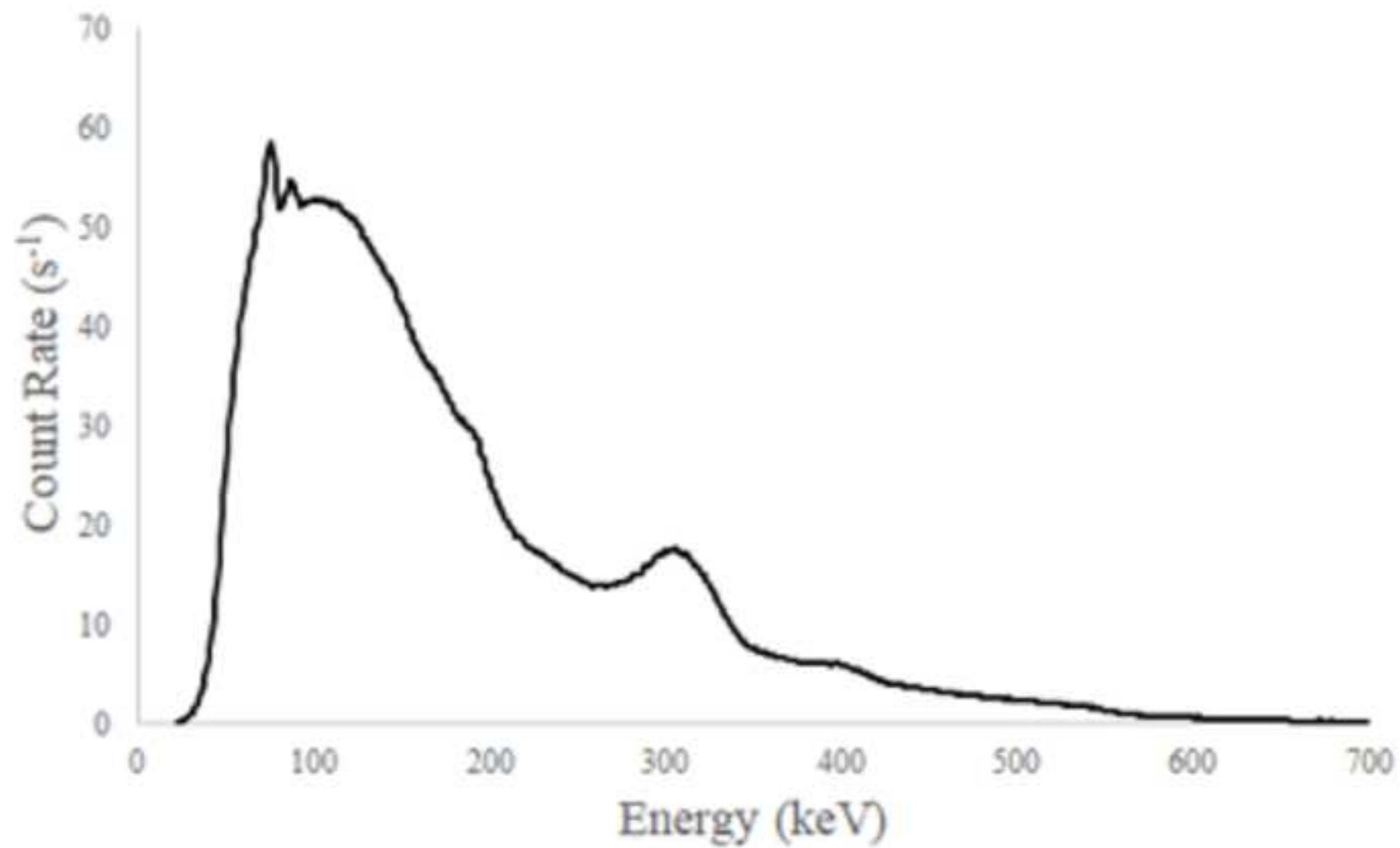


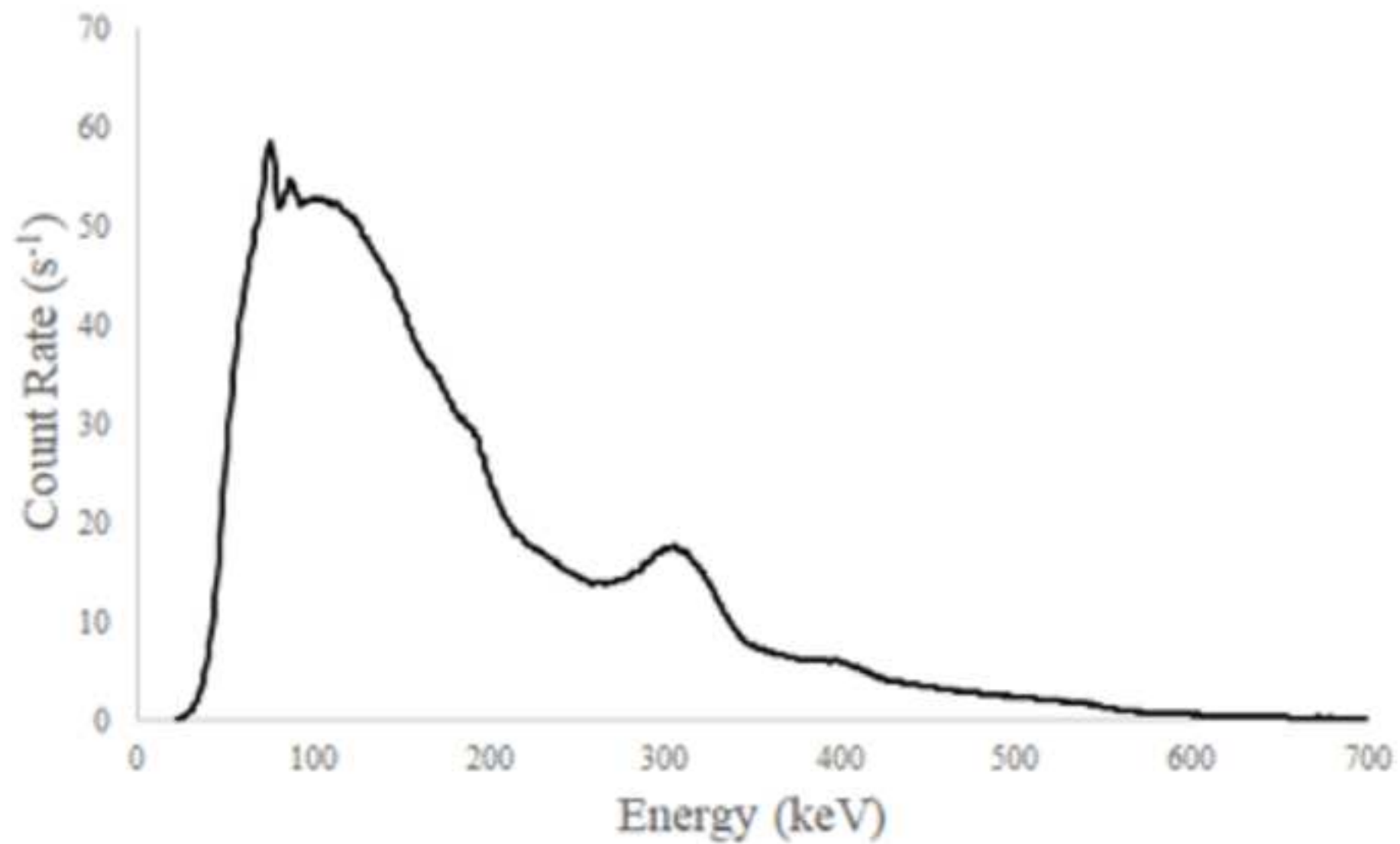


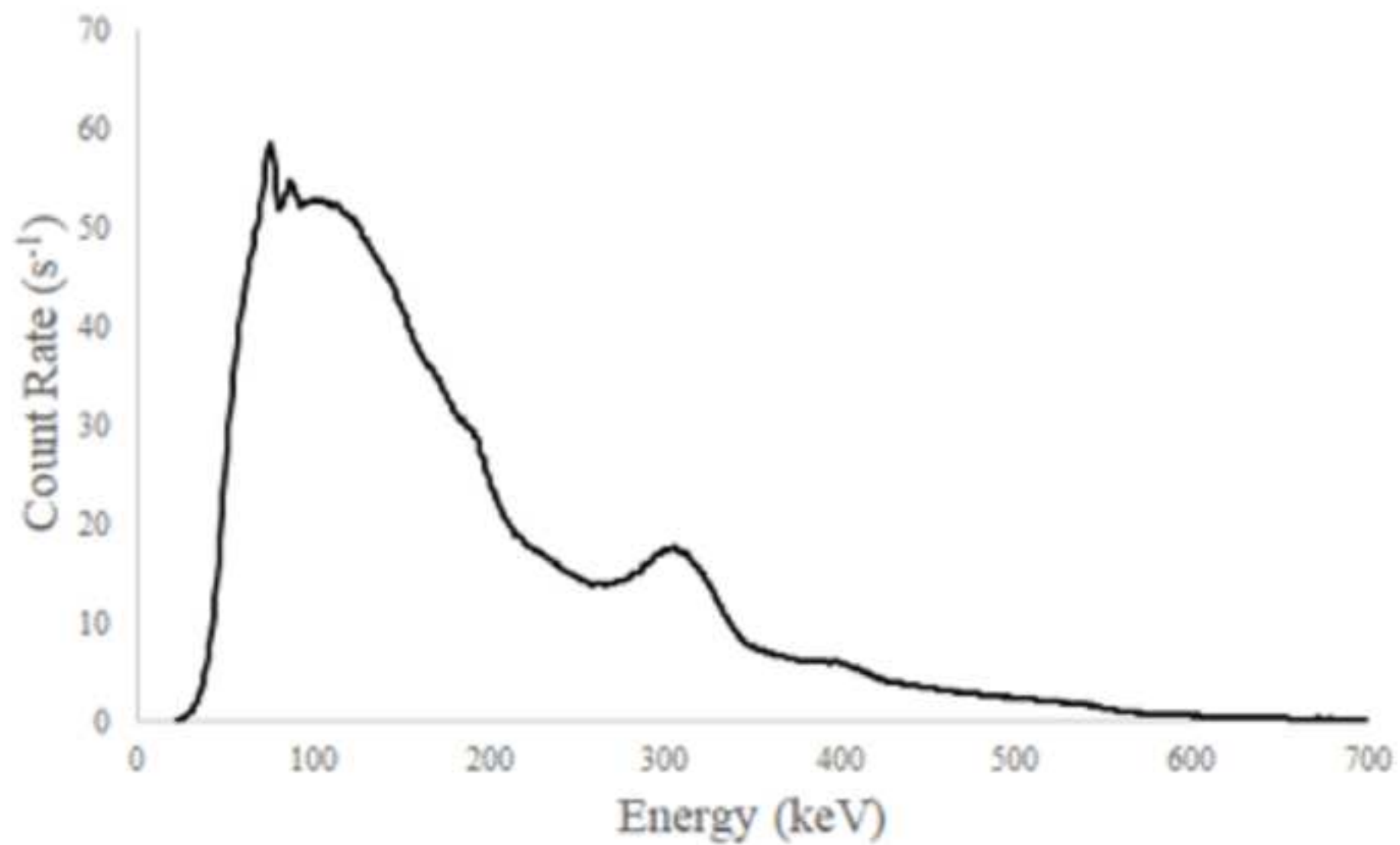


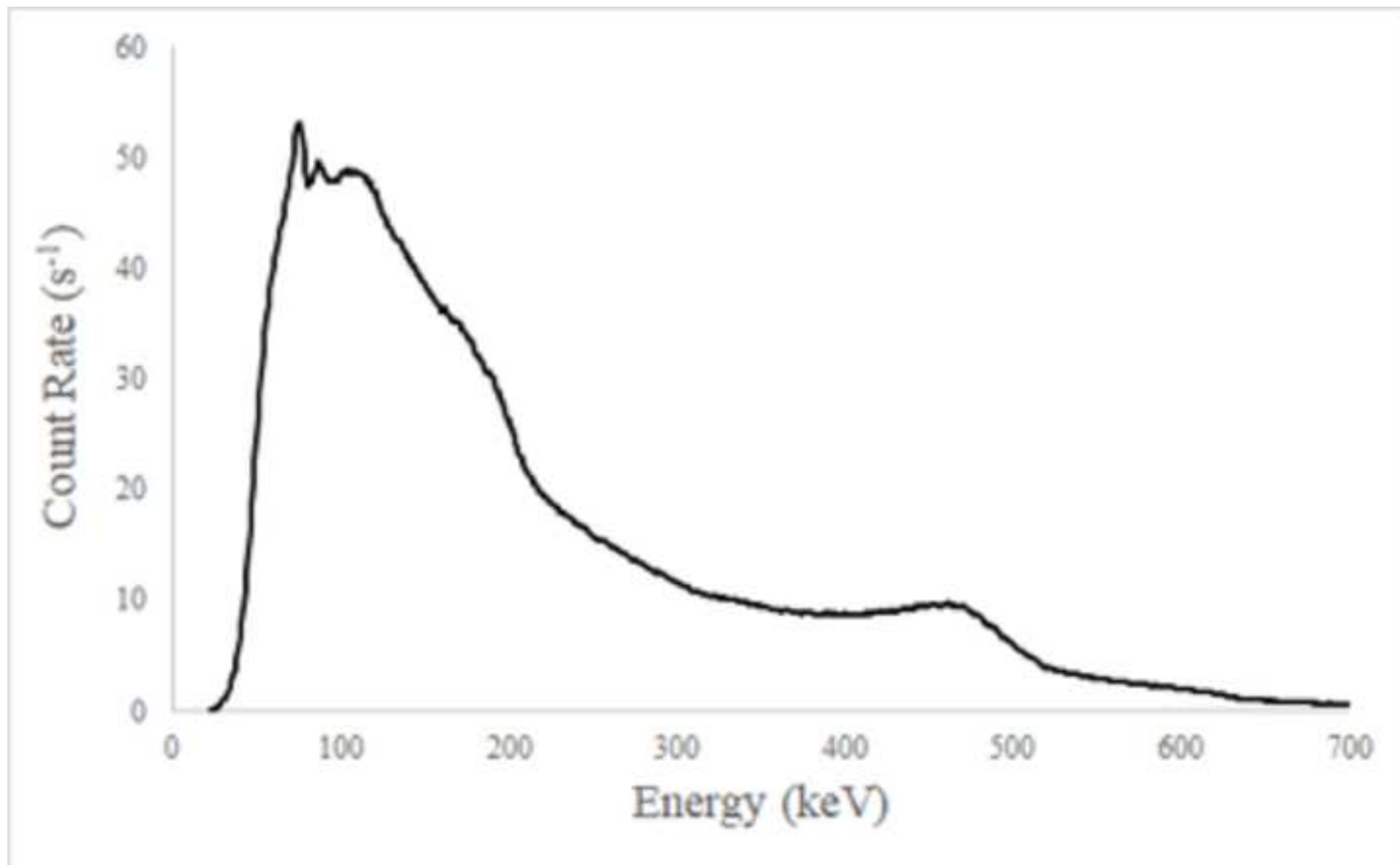


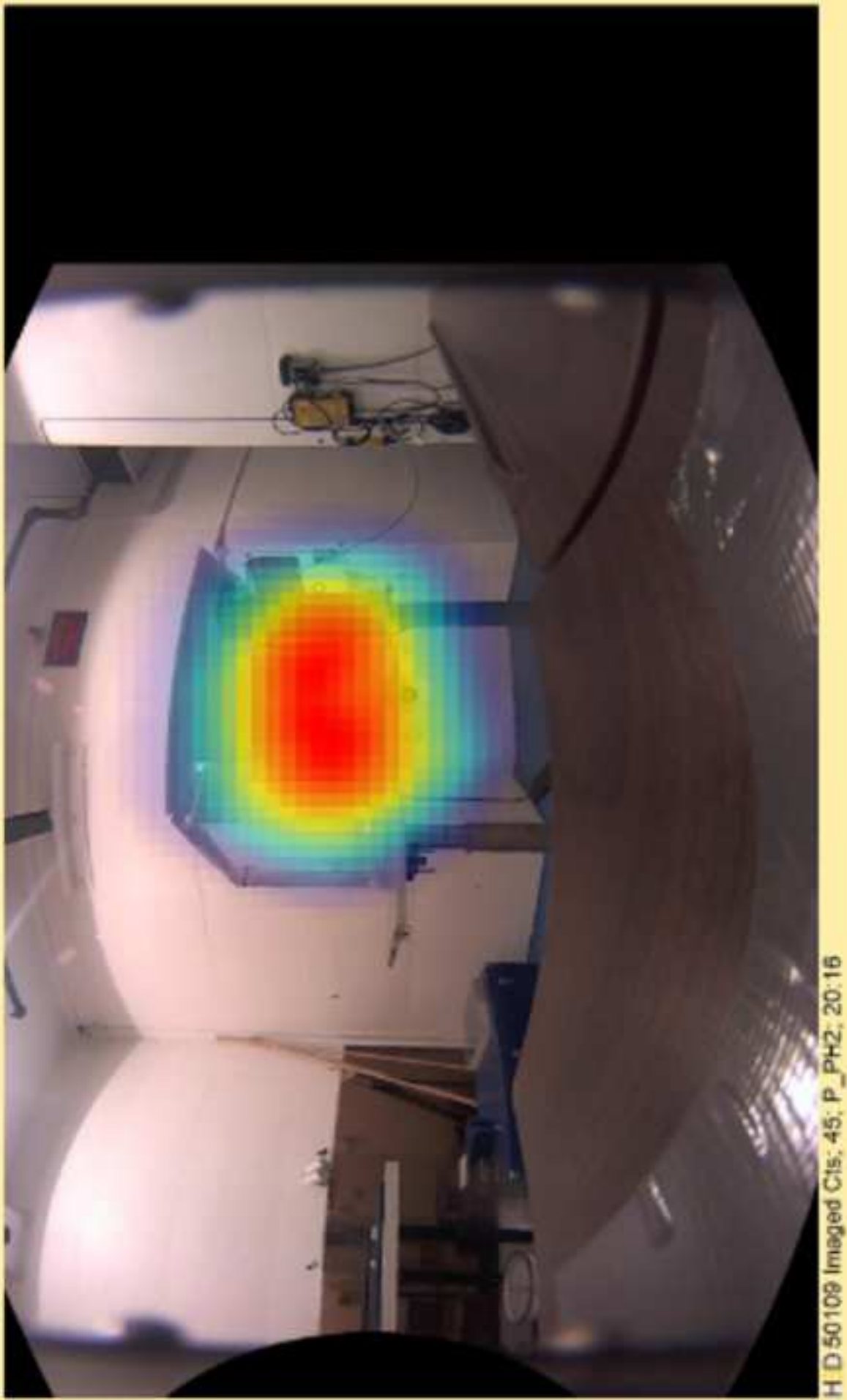


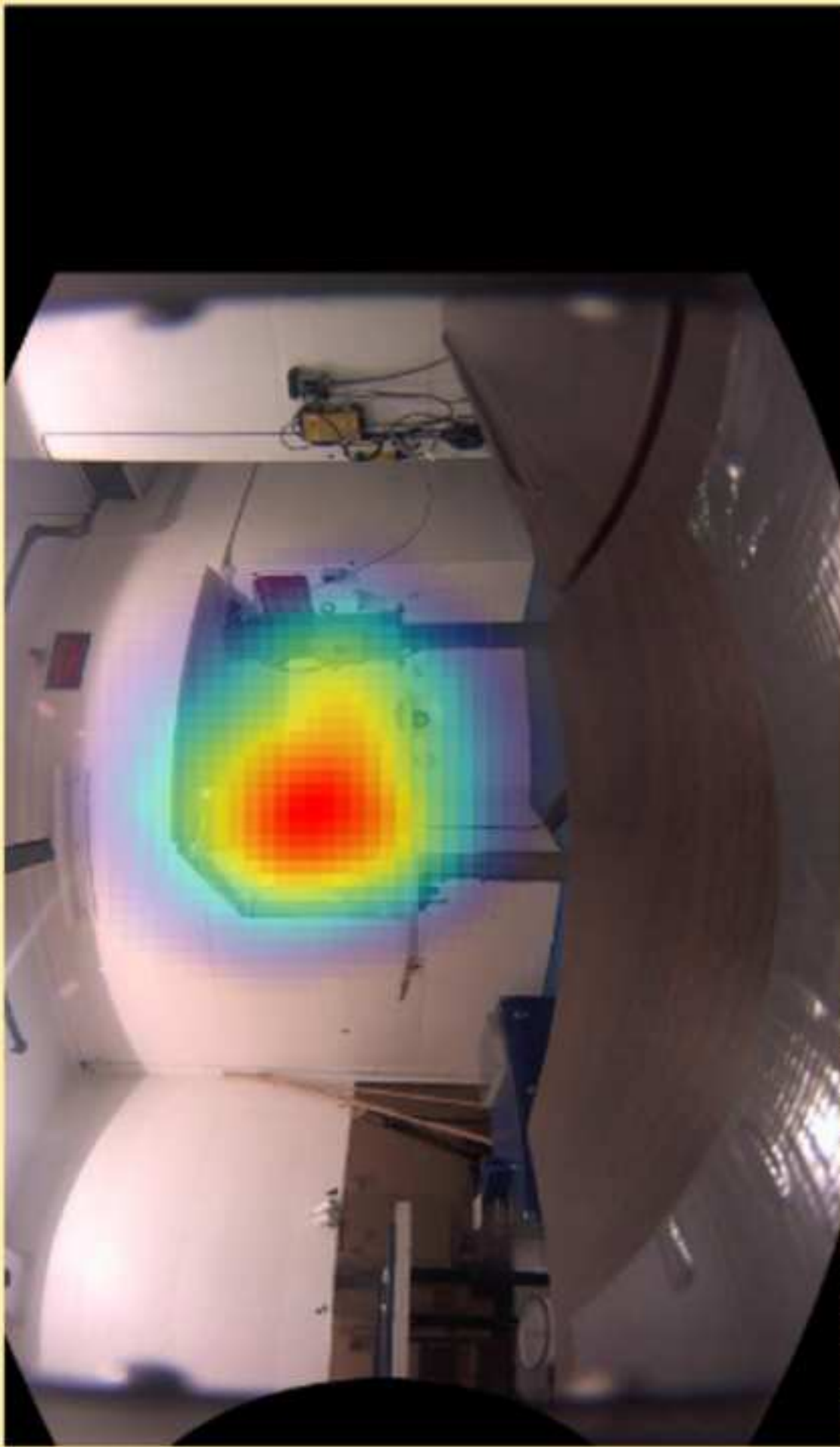




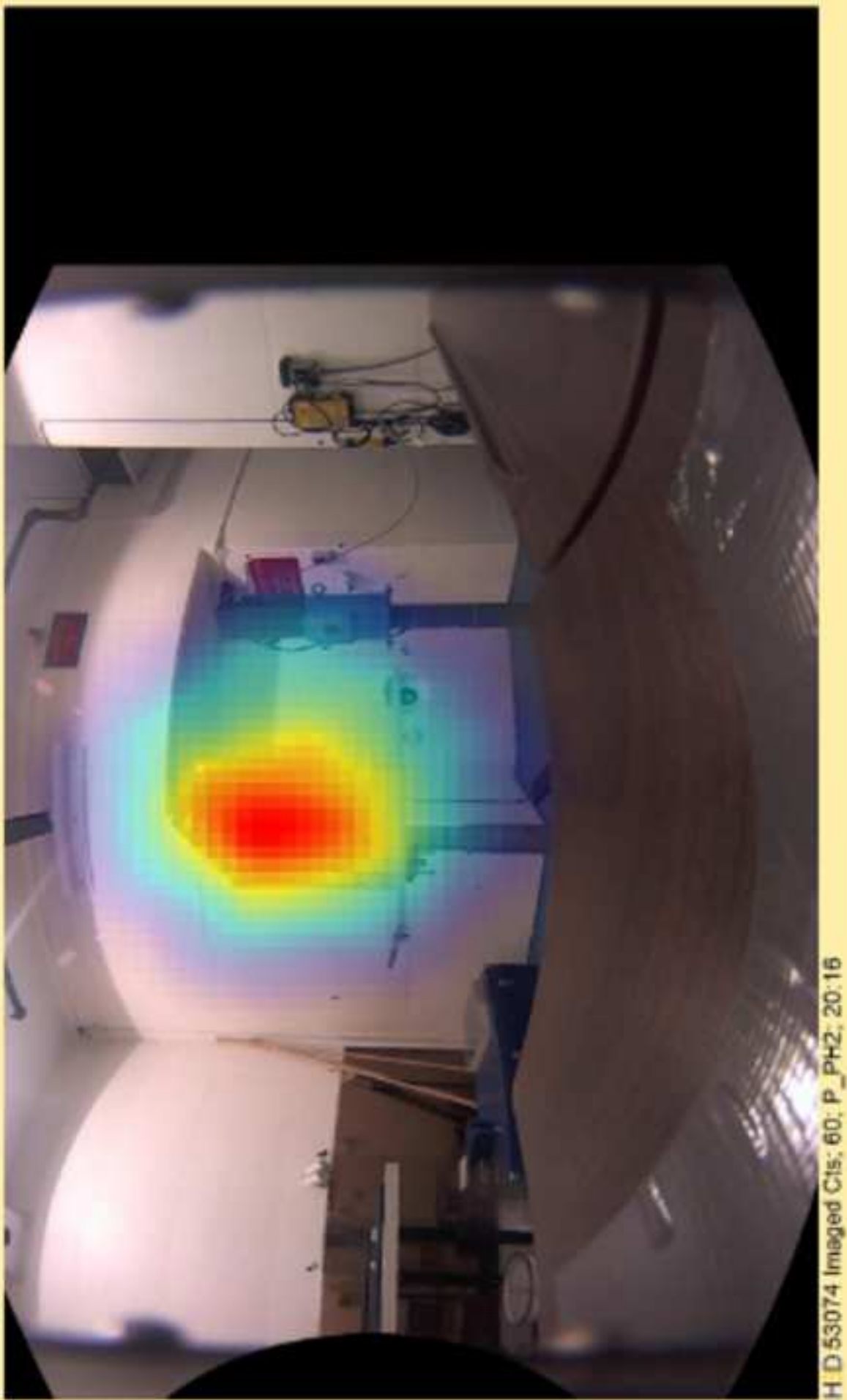


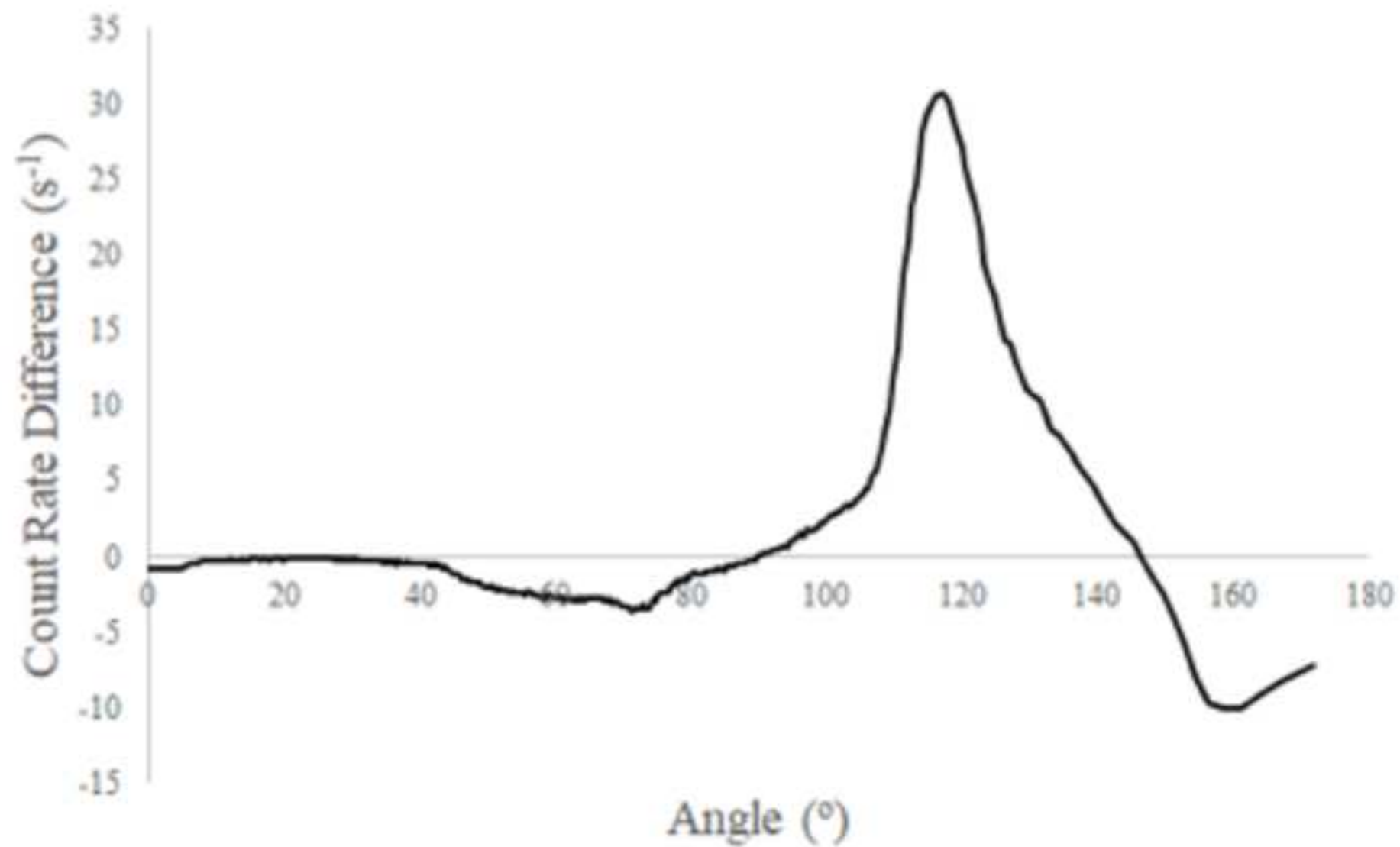


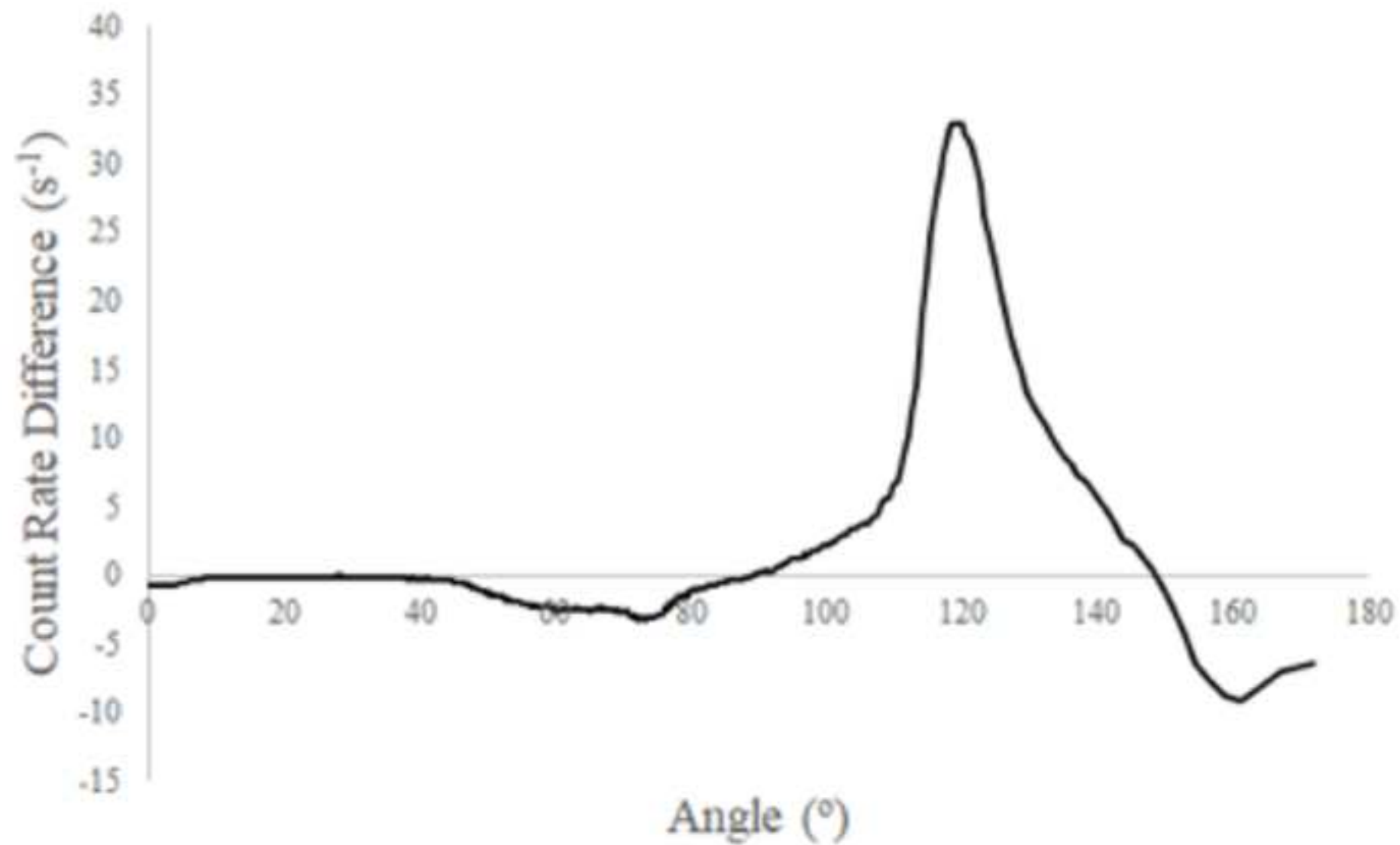


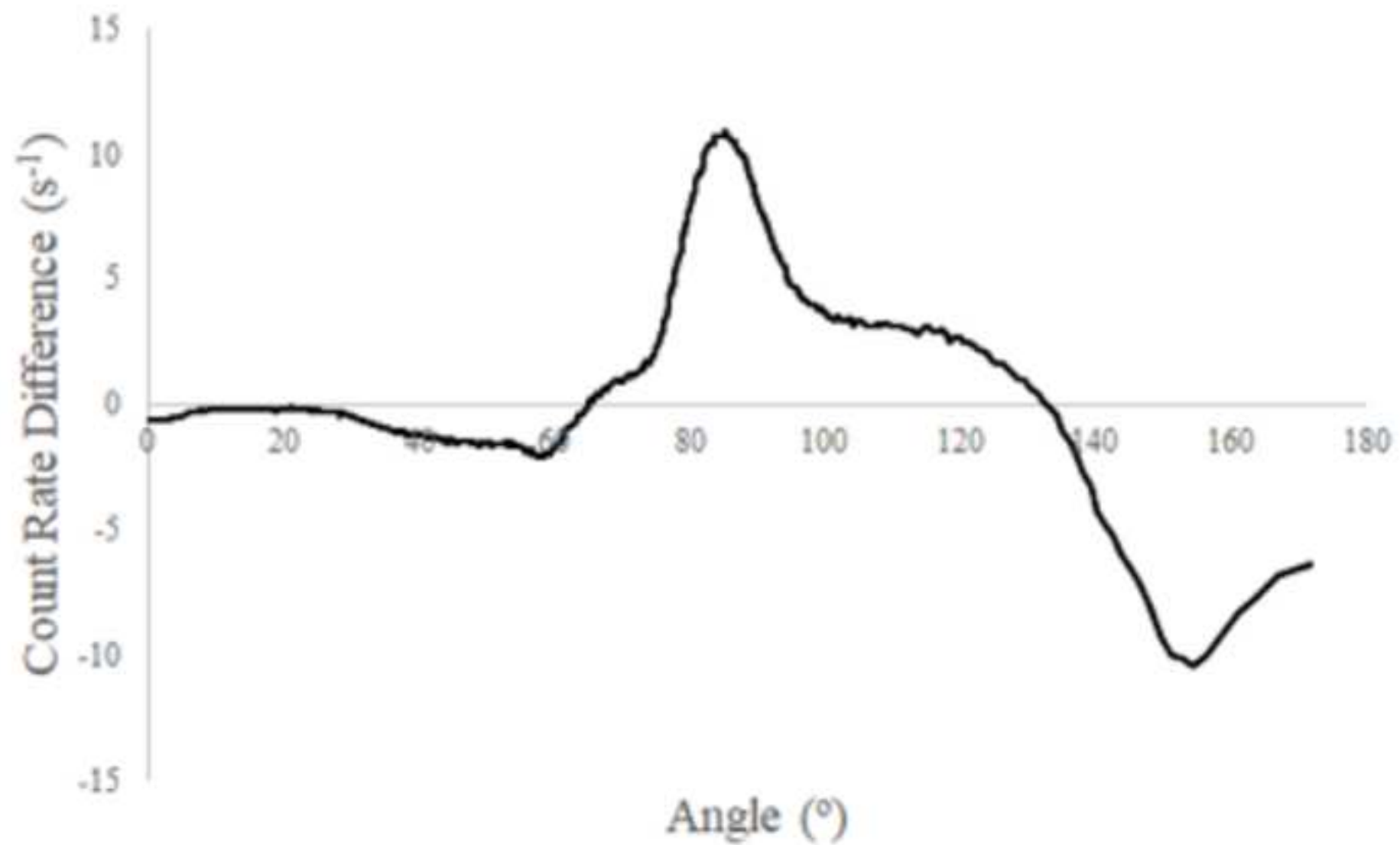


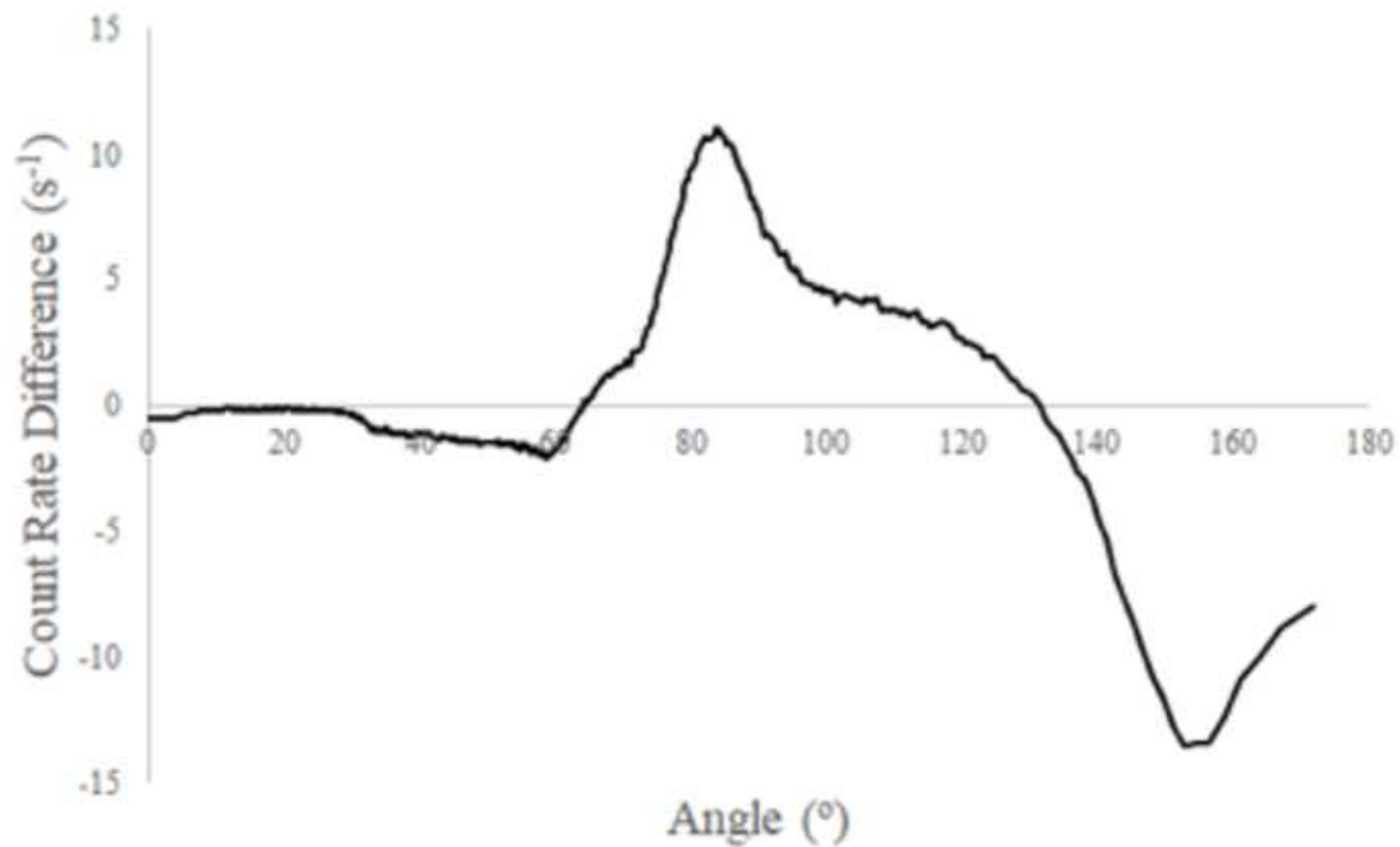
H D 60543 Imaged Cts; 50; P\_P H2; 20:16

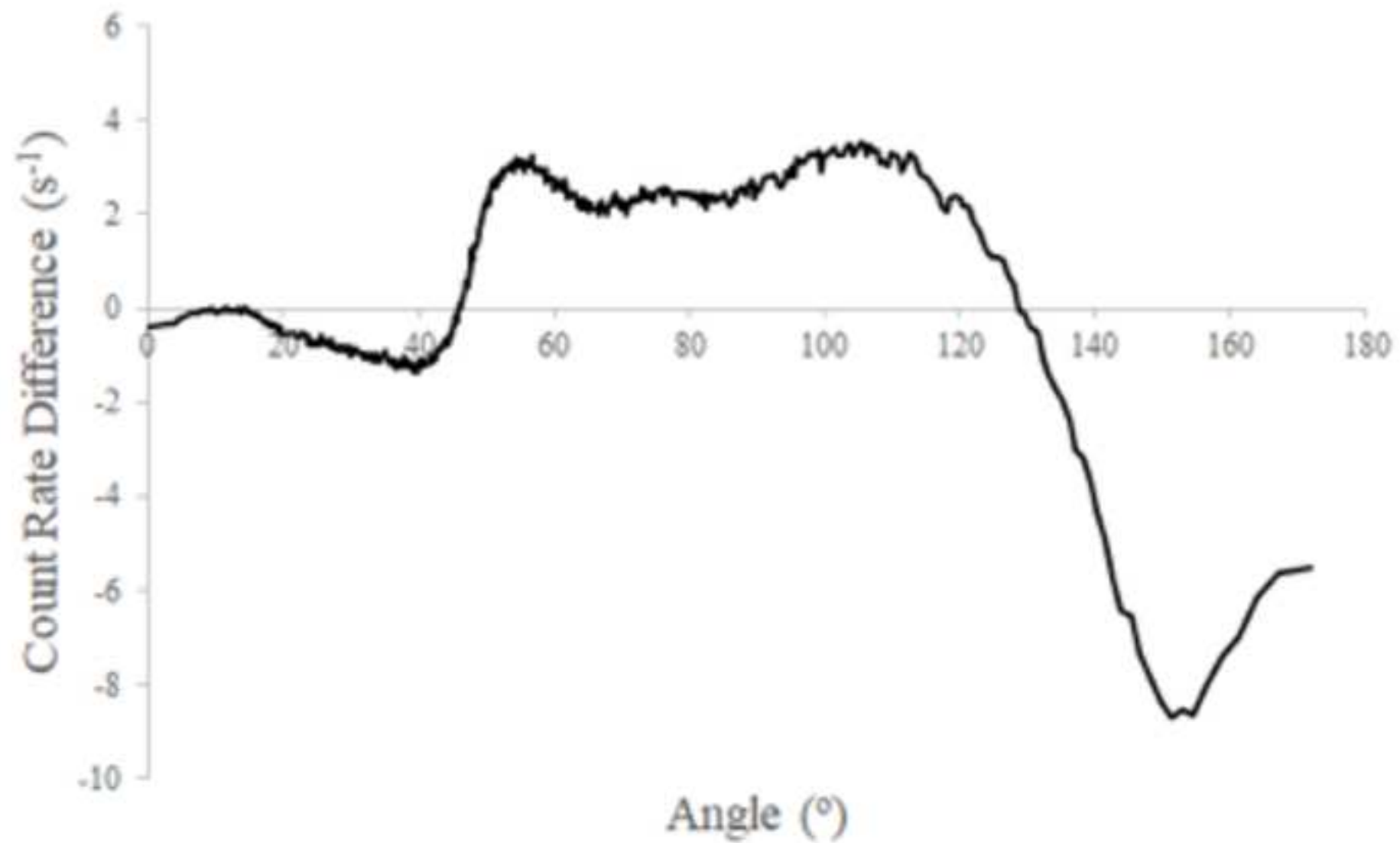


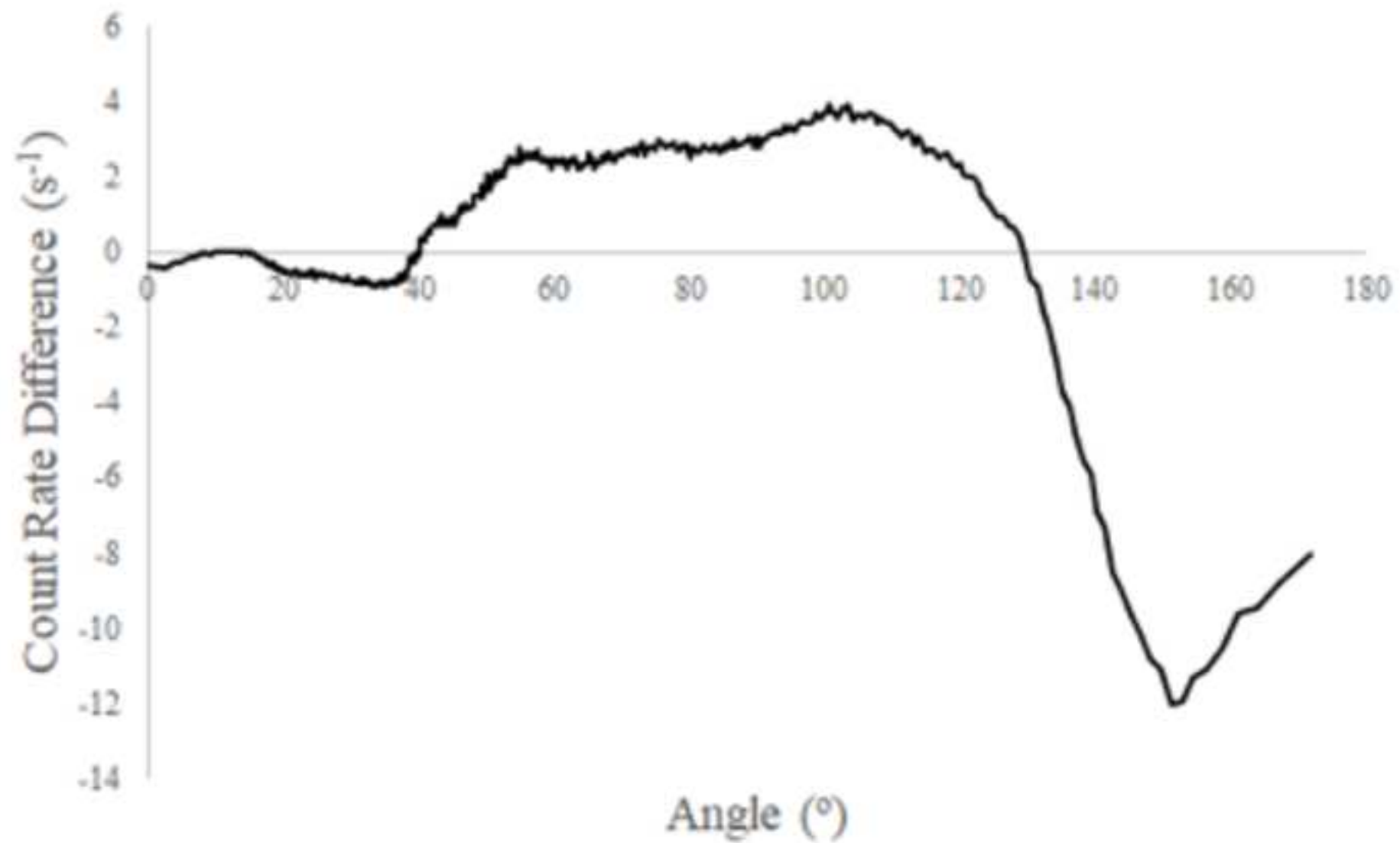


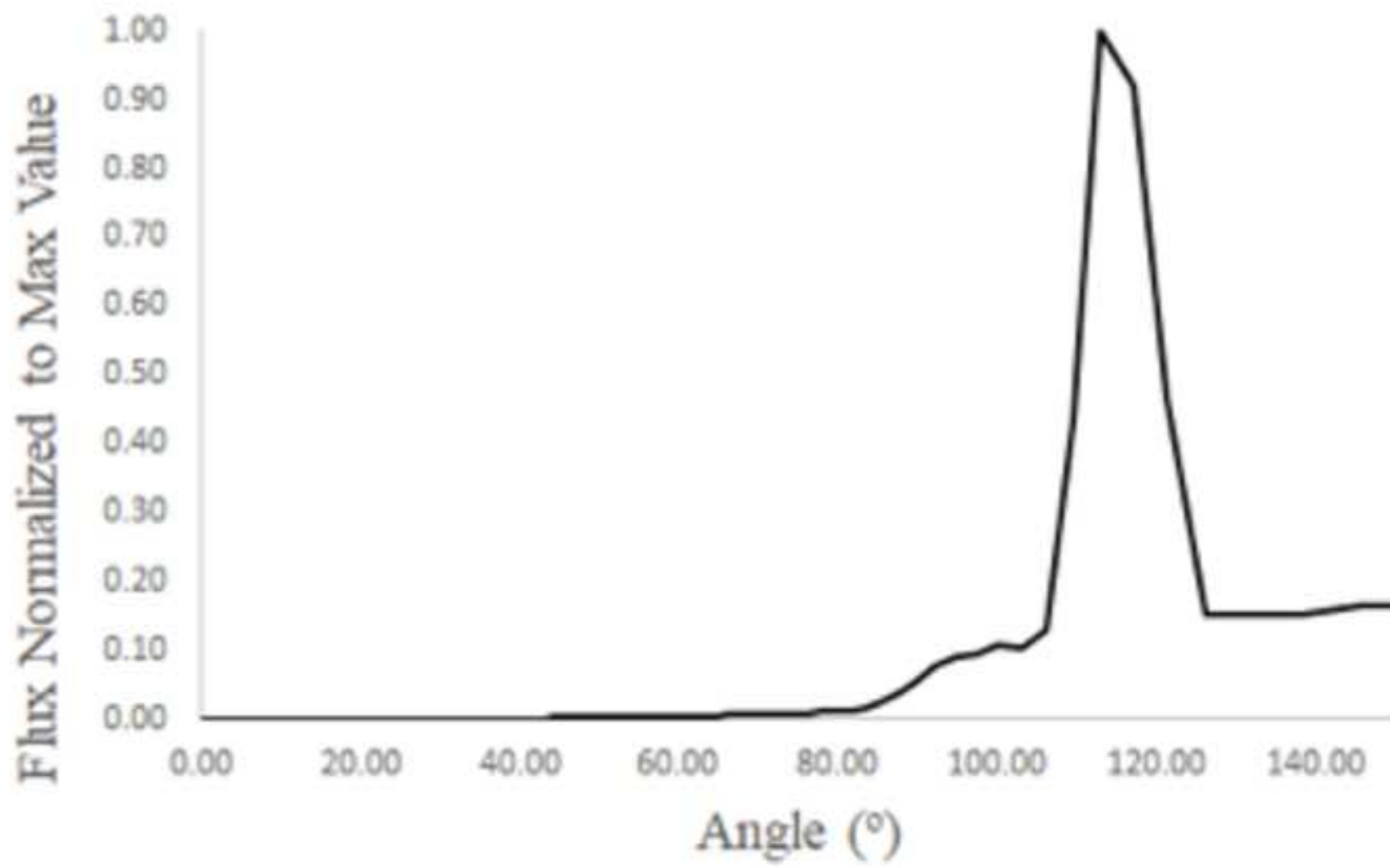


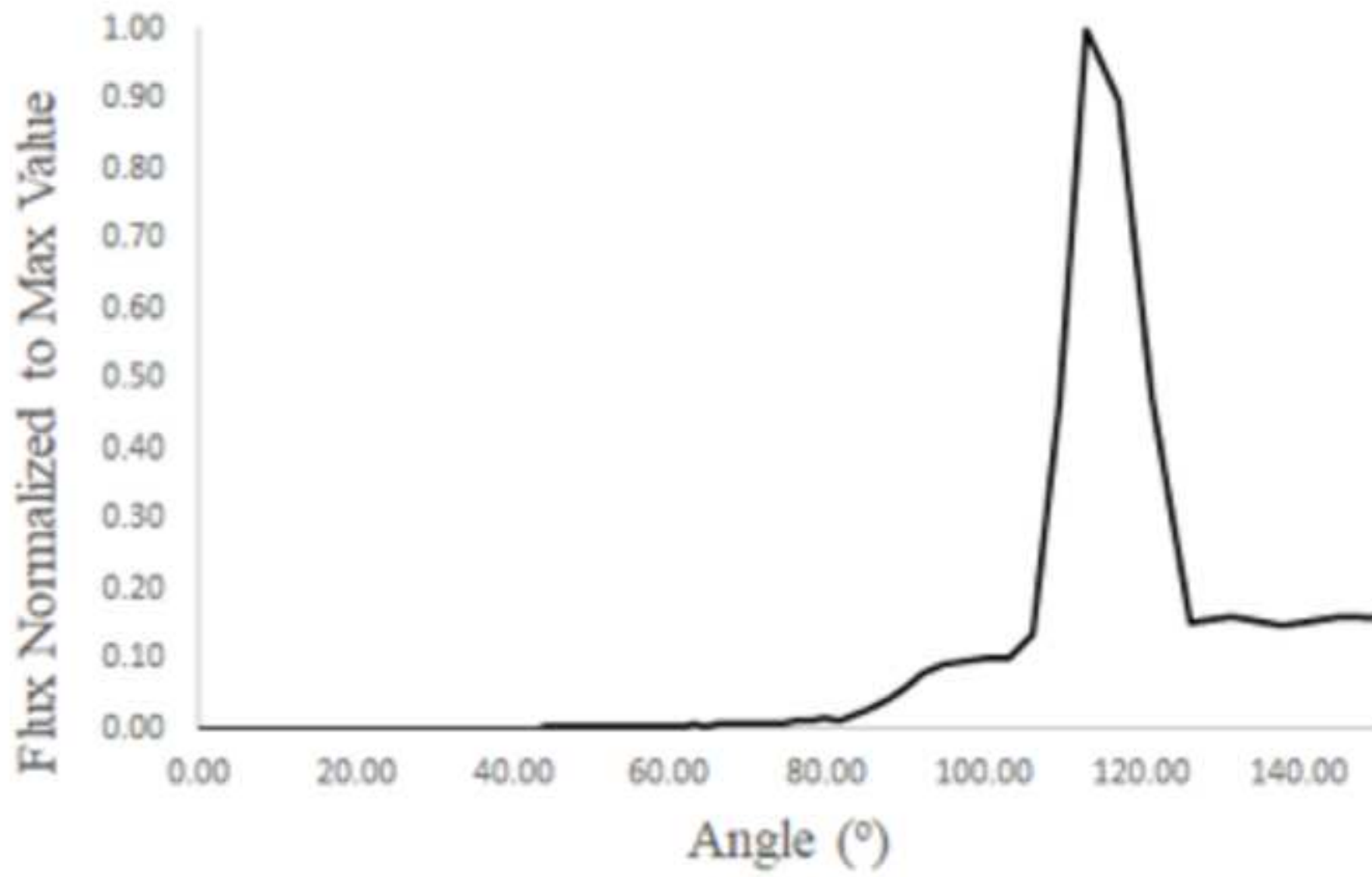


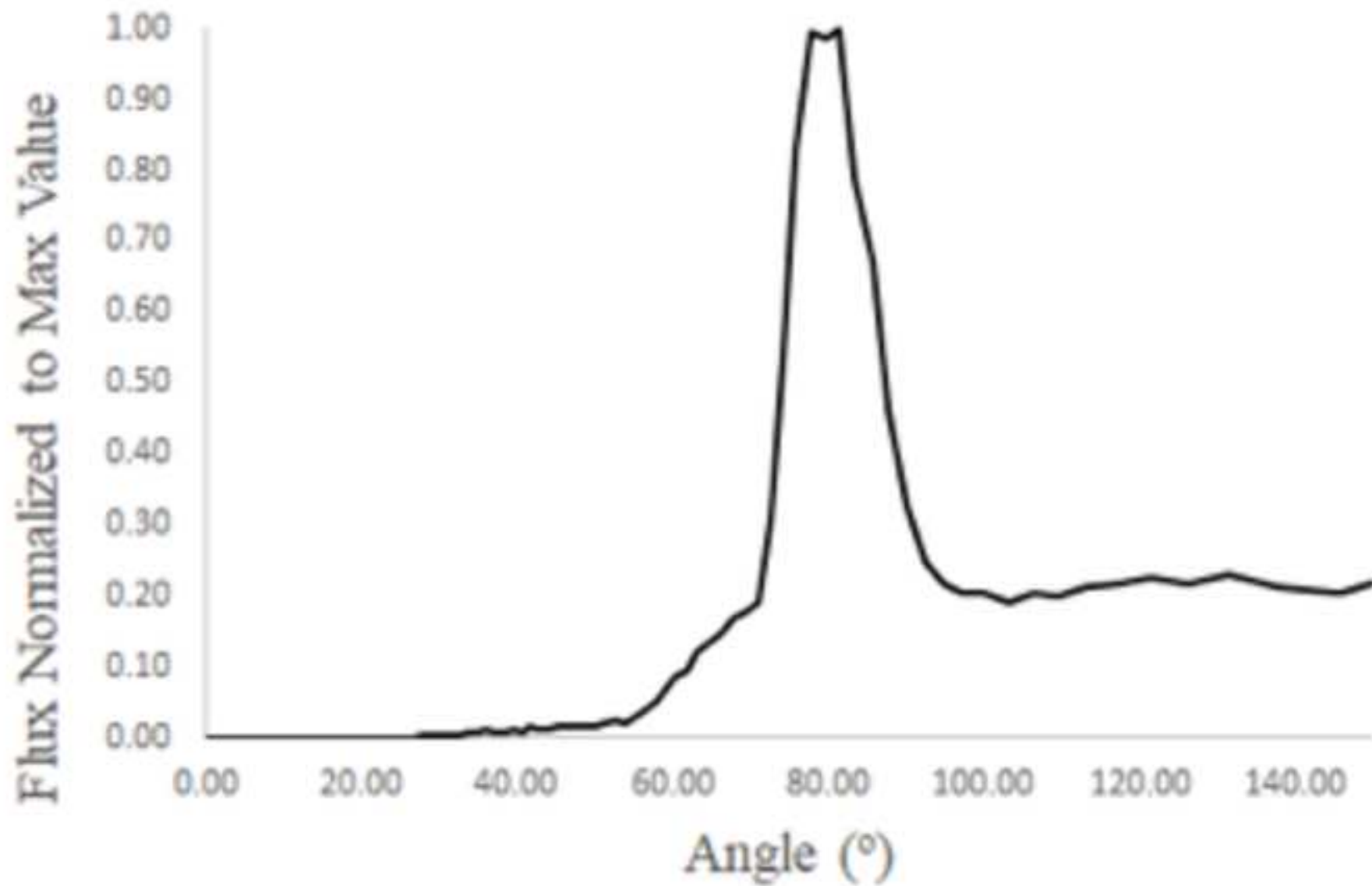


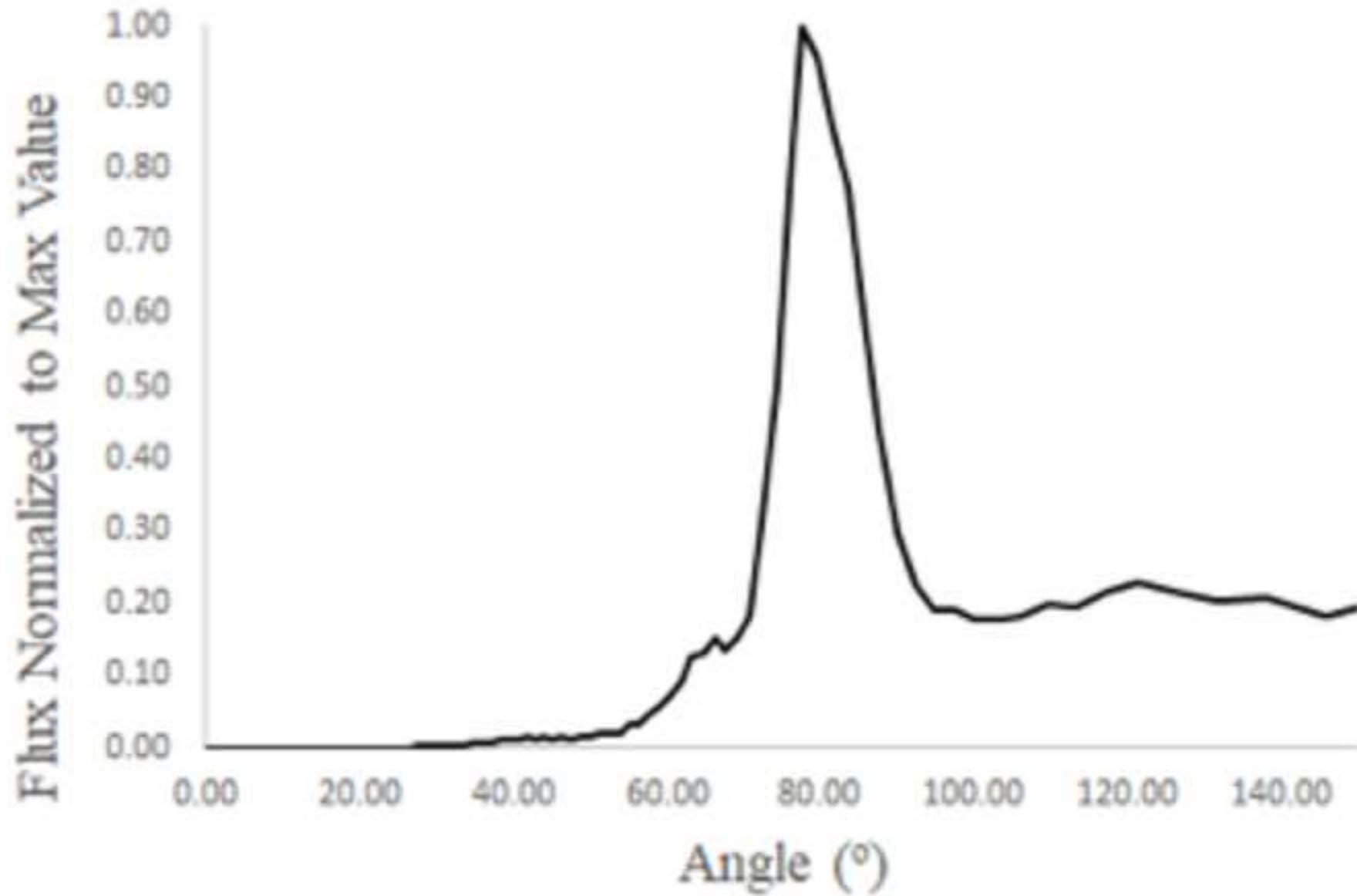


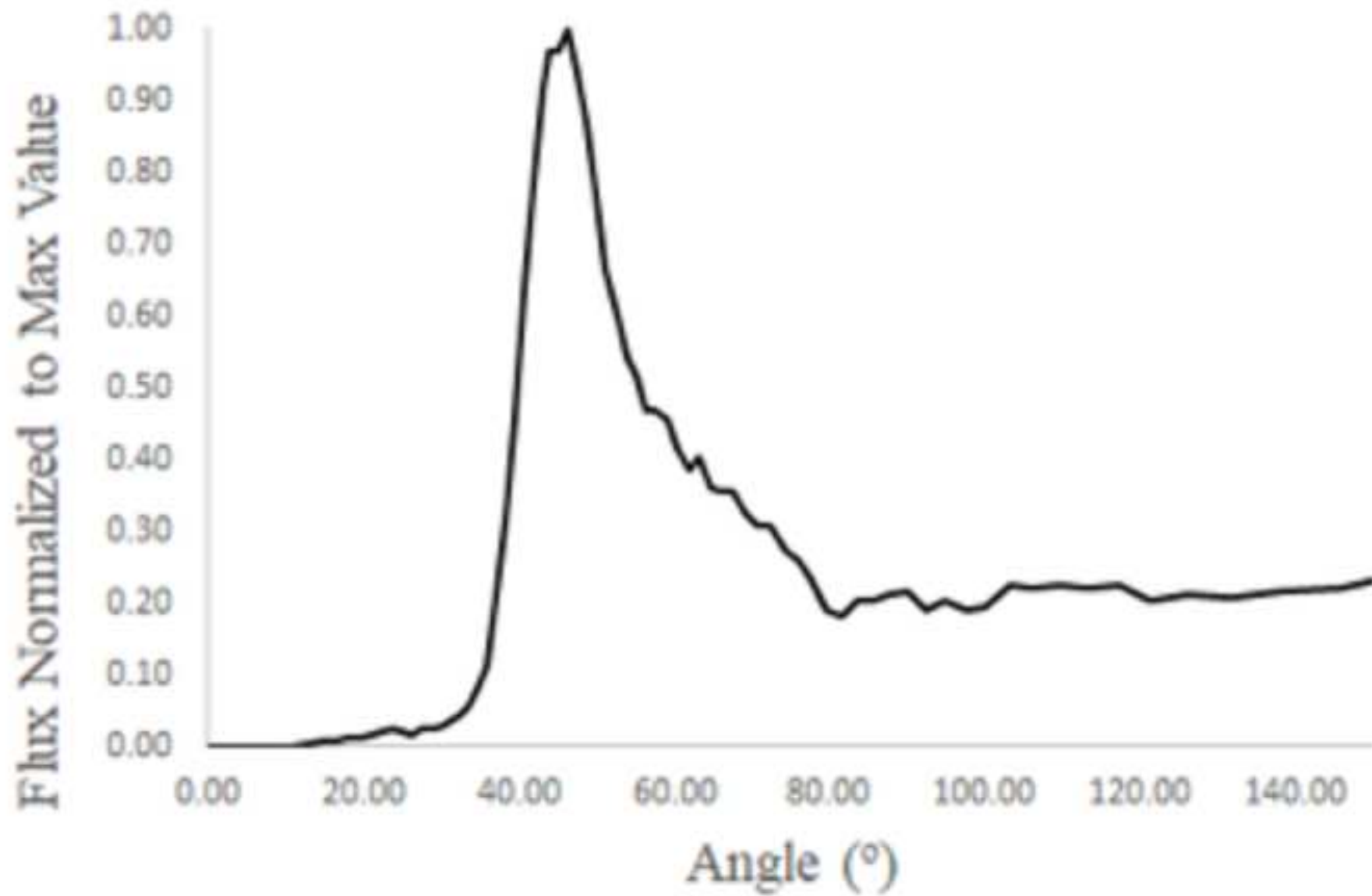


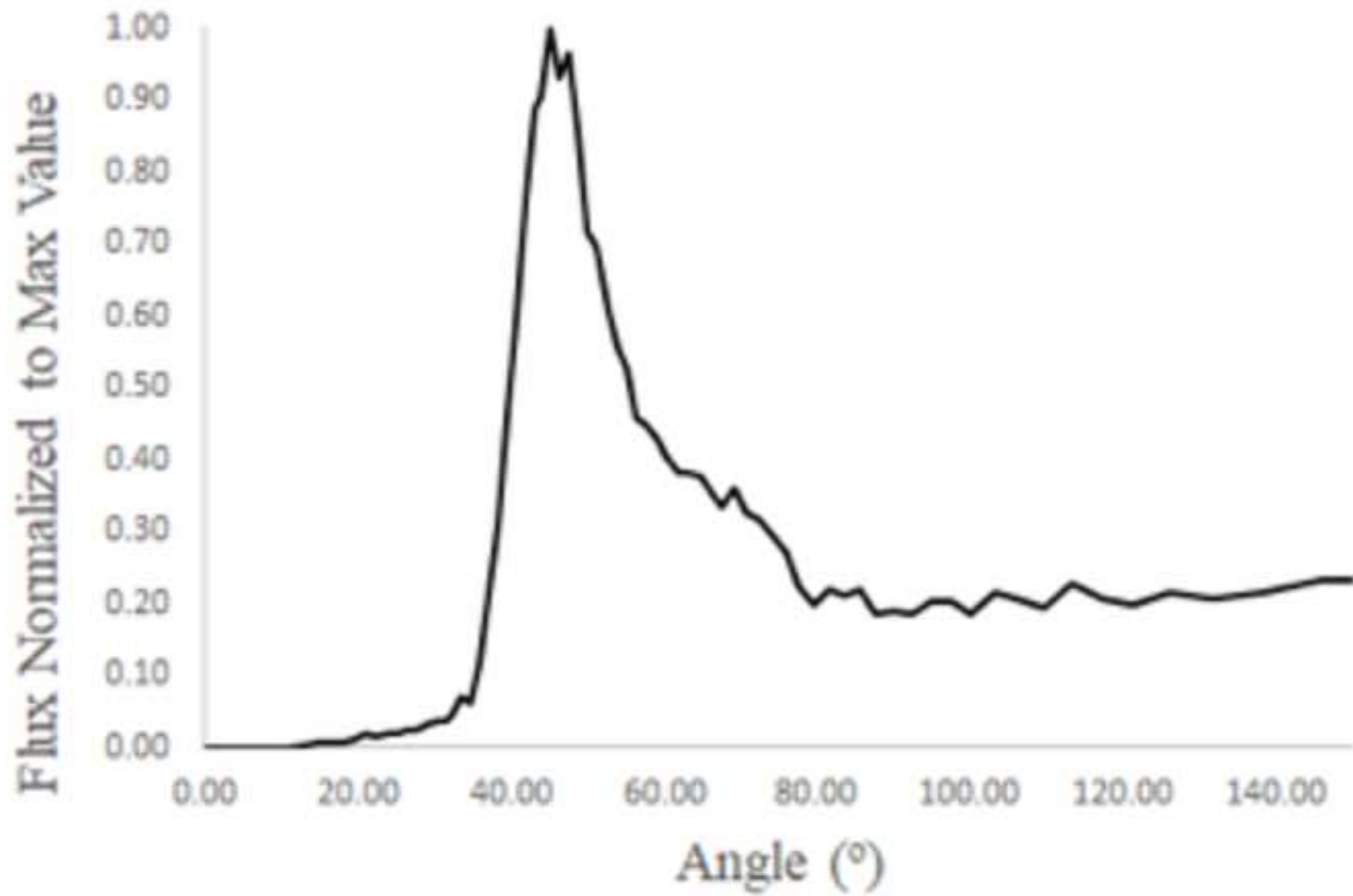












**Paper Summary:** This study demonstrates the usage of a gamma ray imaging spectrometer to better understand the radiation field in a dosimeter calibration facility=.

**Biosketch:** Upon graduation in 2019, Roger Champion hopes to locate a challenging job in the nuclear engineering or radiation protection area. His email is rojochamp@umich.edu.

